CONTRIBUTIONS
OF THE ASTRONOMICAL OBSERVATORY
SKALNATÉ PLESO

• VOLUME LIV •

Number 4

November 2024

CONTENTS

STARS

CELESTIAL MECHANICS

The Contributions of the Astronomical Observatory Skalnaté Pleso
are available in the full version
in the frame of ADS Abstract Service
and can be downloaded in a usual way from the URL address:

https://ui.adsabs.harvard.edu/

as well as from the website of
the Astronomical Institute of the Slovak Academy of Sciences
on the URL address:

https://www.astro.sk/caosp/caosp.php

The journal is covered/indexed by:

Web of Science (WoS)
WoS Core Collection: Science Citation Index Expanded

SCOPUS

Index Copernicus International

Identifying Ae/Be stars in *Gaia* low-resolution BP/RP spectra

E. Paunzen[1] , **M. Prišegen**[2], **S. Hümmerich**[3,4] ,

K. Bernhard[3,4] **and L. Kueß**[5]

[1] *Department of Theoretical Physics and Astrophysics, Faculty of Science,*
Masaryk University, Kotlářská 2, 611 37 Brno, Czech Republic (E-mail:
epaunzen@physics.muni.cz)

[2] *Advanced Technologies Research Institute, Faculty of Materials Science and*
Technology in Trnava, Slovak University of Technology in Bratislava,
Bottova 25, 917 24 Trnava, Slovakia

[3] *Bundesdeutsche Arbeitsgemeinschaft für Veränderliche Sterne e.V. (BAV),*
Berlin, Germany

[4] *American Association of Variable Star Observers (AAVSO), Cambridge,*
USA

[5] *Department of Astrophysics, Vienna University, Türkenschanzstraße 17,*
A-1180 Vienna, Austria

Abstract. Classical Be, and Herbig Ae/Be stars are mainly characterized by emission in the H*alpha* and H*beta* lines. These lines are essential to understanding the formation of massive stars and describing mass loss and stellar winds during stellar evolution. This study aims to characterize and detect classical Be and Herbig Ae/Be stars in *Gaia* BP/RP spectra, which allow us to investigate the complete stellar spectral range. Synthetic Δa and $H\alpha$ index magnitude values were calculated from *Gaia* BP/RP spectra. Colour-colour diagrams were employed to distinguish emission-line objects from normal stars. With the proposed method here, we could unambiguously retrieve 90% of a sample of well-known emission-line objects. This shows that analyzing the 520 nm and $H\alpha$ region efficiently discriminates emission-line objects from normal stars. No further assumptions about astrophysical parameters such as reddening, effective temperature, or IR excess are necessary.

Key words: Techniques: photometric – stars: emission-line, Be – stars: pre-main sequence

1. Introduction

Hot emission-line stars have been the focus of research for a long time. They are ideally suited for studying diverse astrophysical phenomena such as mass

loss, circumstellar disks or shells, and pulsation. With the advent of large-scale spectroscopic surveys such as the Sloan Digital Sky Survey (SDSS; Blanton et al., 2017; Abdurro'uf et al., 2022) and the Large Sky Area Multi-Object Fiber Spectroscopic Telescope (LAMOST; Zhao et al., 2012; Cui et al., 2012) surveys, the research on these objects has seen a significant boost (e.g. Anusha et al., 2021; Shridharan et al., 2021; Zhang et al., 2022).

A diverse set of objects is lumped together under the heading of hot emission-line stars, such as the classical Be and B-type shell stars, young stellar objects like Herbig Ae/Be stars, B[e] stars, supergiants, mass transferring binaries or Wolf-Rayet stars (e.g. Rivinius et al., 2013).

Classically, Be stars are defined as stars that are not supergiants and show or have shown emission features in at least one Balmer line at least once (Collins, 1987). The observed emission features are mostly due to equatorial disks produced by stellar winds. Depending on the inclination one looks at the star, sometimes a narrow absorption feature is present in the emission line. This effect is less prominent when looking at the star's polar regions and gets stronger the closer one is to the equator (Slettebak, 1979; Rivinius et al., 2013). In addition, photometric variability on different timescales is commonly observed in these stars. Periodic variations on intermediate time scales (days to months) cannot be explained by non-radial pulsation, although the beating of closely spaced non-radial pulsation frequencies have been postulated as a possible explanation (Labadie-Bartz et al., 2017). Photometric variability on long time scales (months to decades) is generally attributed to (changes in) the circumstellar disc, most notably its development and dispersion. Discs are created through events referred to as outbursts, in which mass is elevated from the stellar surface and the development of, and mass transfer to, the disc is initiated. Outbursts are accompanied by characteristic photometric variations (e.g. Rivinius et al., 2003; Porter & Rivinius, 2003; Kurfürst et al., 2018). Emission phases may be replaced by shell and normal phases in the same object.

We here present our efforts at characterizing and finding hot emission-line stars in *Gaia* low-resolution BP/RP spectra (Carrasco et al., 2021; De Angeli et al., 2022) using a pre-selected sample of classical Be and Herbig Ae/Be stars as reference. This will help in the future detection of emission line stars even in spectra with (extremely) low spectral resolution such as the *Gaia* BP/RP spectra of *Gaia* DR3 and forthcoming data releases. Our method can be a new criterion for detecting such stars.

2. Target selection

We selected all Herbig Ae/Be and classical Be stars from the catalogues of Jaschek & Egret (1982), Bernhard et al. (2018), and Vioque et al. (2020) for which a BP/RP spectrum is available. Our sample consists of 794 objects with $3.2 < G < 12.7$ mag.

For the control sample of apparently normal stars, we chose all objects included in the paper by Paunzen & Prišegen (2022) and extended this sample with stars from Paunzen et al. (2005). This sample of stars has non-peculiar Δa values and can be used as a standard and reference.

Δa-photometry is a powerful tool in detecting magnetic chemically peculiar (mCP) stars (Paunzen et al., 2005). It uses the flux-depression at λ5200 (Kodaira, 1969) to do so. The method uses three narrowband filters: one to the left of the depression (g_1), one right on the depression (g_2), and one on the right of the depression (y). From the (synthetic) magnitudes in these filters, the peculiarity index a can be calculated:

$$a = g_2 - \frac{(g_1 + y)}{2}. \tag{1}$$

This quantity, however, is slightly colour/temperature dependent, and thus a Δa value is calculated as such:

$$\Delta a = a - a_0(g_1 - y). \tag{2}$$

All stars that lie more than 3σ above the "normality line" a_0 have a significant flux depression and can be taken as candidate peculiar stars.

We selected 435 stars of spectral types B0 to F7 with luminosity classes V to III. The astrophysical parameter space of stars beyond the zero-age main sequence should cover the entire pre-main sequence region (Haemmerlé et al., 2019). We note that both samples also include binary stars.

No cut according to the signal-to-noise ratios of the spectra was applied for both samples.

3. Methods and Results

To calculate the synthetic magnitudes, we first normalized all spectra to unity at a common wavelength of 402 nm. All spectra were brought to the same absolute flux at this wavelength region. No additional normalization was performed in the region of Hα. This technique was successfully applied to the synthetic Δa photometry (Sect. 3.1.) Applying a standard polynomial technique, the spectra were then interpolated to a one-pixel resolution of 0.1 nm in the wavelength regions from 480 to 580 nm and 610 to 700 nm. No further smoothing or cleaning algorithms were used. Each filter curve was folded with the corresponding spectrum as described in Stigler et al. (2014). The final magnitudes for all filters are in arbitrary units.

The calculated Δa and Hα index magnitude values for the sample of known Herbig Ae/Be and classical Be stars are presented in a text file provided as supporting material. The first ten rows are shown in Table 1 for guidance regarding the text file's form and content. *Gaia* data were gleaned from DR3 (Gaia Collaboration et al., 2016; Babusiaux et al., 2022; Gaia Collaboration et al., 2022).
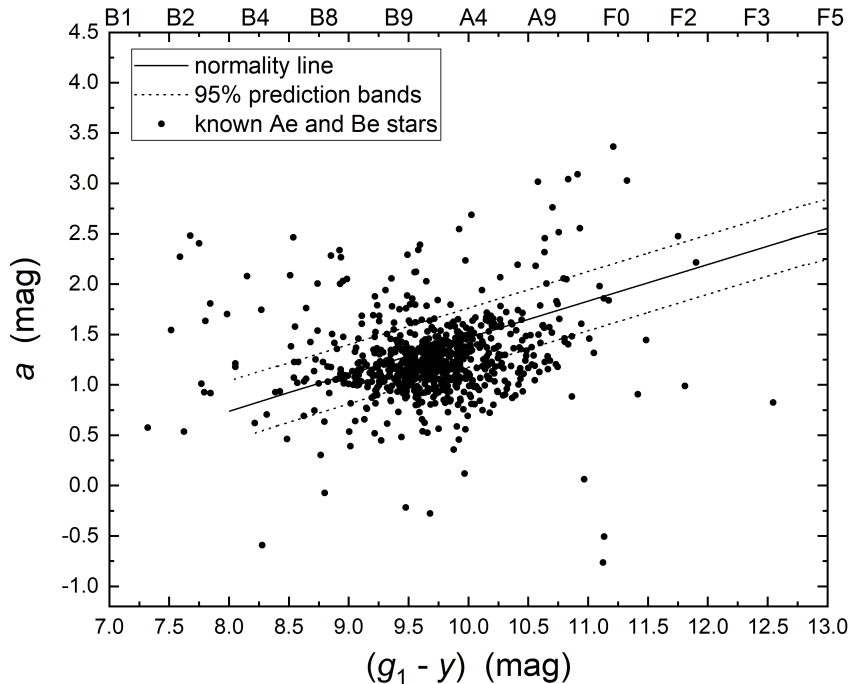
Figure 1. The sample of known Herbig Ae/Be and classical Be stars in the a versus $(g_1 - y)$ magnitude parameter space. As expected, most objects do not show any significant deviations from the normality line (solid line) and the 95% prediction bands for the standard stars (dotted lines; from Paunzen & Prišegen, 2022). Stars above the normality line are in the shell phase, and stars below are in the emission phase.

3.1. Δa photometry

Pavlovski & Maitzen (1989) analysed the different phases of classical Be stars within the Δa photometric system. They investigated, in particular, the case of Pleione, which is quite outstanding. It reached a Δa value of $+36$ mmag in the shell phase and dropped quite rapidly to zero within a year. Detailed measurements for 59 objects were presented by Paunzen et al. (2005) with extreme values for the emission phase of -19 mmag. The negative Δa values found are caused by emission in iron and magnesium lines (Hanuschik et al., 1996).

We used the three filters defined in Paunzen & Prišegen (2022) with a bandwidth of 13 nm and central wavelengths of g_1 (501 nm), g_2 (521.5 nm), and y (548.5 nm).

In Fig. 1, the results for the sample of known Herbig Ae/Be and classical Be stars are shown, together with the normality line and its 95% prediction bands.

Several extreme outliers were omitted from the plot. The objects show the same behaviour as the ones published by Paunzen et al. (2005, see Fig. 5 therein), who employed classical photoelectric Δa photometry. From the 794 objects, 95 (12%) are above and 194 (24%) below the corresponding 95% prediction bands. Thus, almost two-thirds of the classical Be and Herbig Ae/Be stars cannot be detected at the 520 nm region. Nevertheless, a significant negative or positive Δa value can help to corroborate the results from the Hα region.
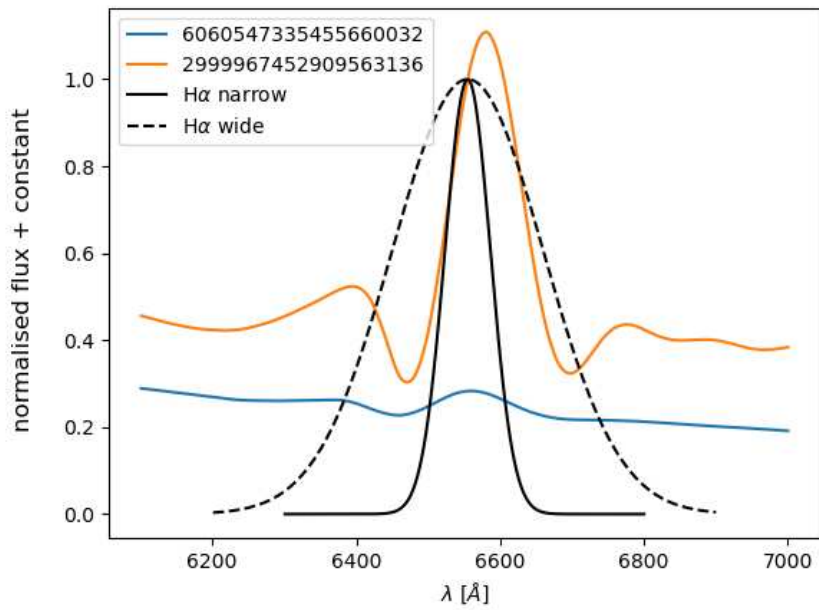
Figure 2. Filter curves used to probe the Hα line. Also shown are two example spectra which were offset by a constant value. The lower blue spectrum belongs to a star with some Hα emission (*Gaia* DR3 6060547335455660032). The upper orange spectrum shows a very strong emission feature (*Gaia* DR3 2999967452909563136).

3.2. Hα photometry

One of the main characteristics of classical Be and Herbig Ae/Be stars is the variability of the hydrogen lines, which manifests itself especially in the Hα and Hβ lines. On very different time scales, these lines are observed in strong emission or absorption as in normal stars. Another essential aspect is the vari-
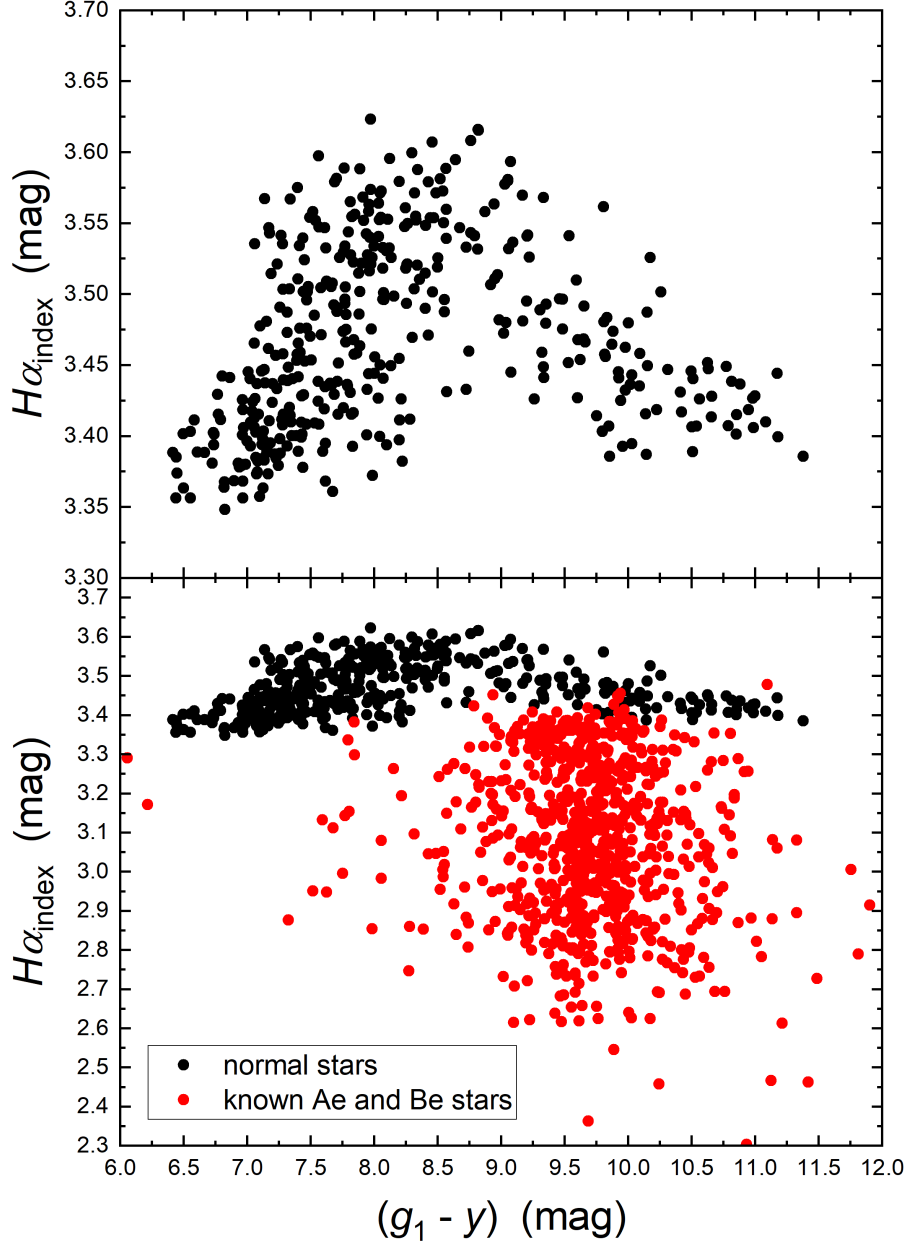
Figure 3. The samples of normal stars (filled black circles) and known Herbig Ae/Be and classical Be stars (filled red circles) in the Hα index versus $(g_1 - y)$ magnitude parameter space. Any object with Hα index < 3.35 over the full colour (effective temperature) range is assumed to show emission in the Hα line.

Table 1. Elementary data for the sample of known Herbig Ae/Be and classical Be stars. The columns denote: (1) *Gaia* DR3 identifier. (2) 2MASS identifier (Skrutskie et al., 2006). (3) Right ascension (J2000; *Gaia* DR3). (4) Declination (J2000; *Gaia* DR3) (5) *G*-band mean magnitude (*Gaia* DR3). (6) Calculated $(g1 - y)$ colour index. (7) Calculated Δa value. (8) Calculated Hα value.

(1) Gaia_ID	(2) 2MASS_ID	(3) α(J2000)	(4) δ(J2000)	(5) G mag	(6) $(g1 - y)$	(7) Δa	(8) Hα
1384384649468452224	15553059+4233582	238.877325	42.566264	5.6984	9.504	-0.003	3.386
1741560280196688000	21352379+0929184	323.849126	9.488430	10.0942	9.388	$+0.077$	3.132
1808447386454770304	20170976+1552215	304.290707	15.872623	7.5656	10.151	$+0.143$	3.174
1817679706409974400	20383016+2119439	309.625721	21.328888	9.2816	8.935	$+0.069$	3.172
1824520940823718656	19465768+1814559	296.740351	18.248855	10.4601	9.489	$+0.602$	3.379
1826951544369716480	20024644+2151160	300.693478	21.854407	8.2510	9.980	-0.403	2.928
18370970560174259	05254477+3538499	81.436597	35.647184	8.1591	7.624	-0.071	2.949
18449747132375206	05223522+3740336	80.646805	37.675993	7.2317	10.032	-0.459	2.827
1849597571190605952	21354448+2944439	323.935321	29.745477	8.0383	9.422	-0.265	2.639
185767888290202880	05095643+3700158	77.485137	37.004430	8.2110	9.952	-0.171	3.129

ability of the line-profiles, which may show different shapes within a few hours or remain stable over a timescale of years (Catanzaro, 2013).

To identify emission-line objects, we chose an approach similar to the calculation of the Hβ index in the Strömgren-Crawford system (Strömgren, 1966). The idea is to measure the flux of the entire Hα line and compare this to the flux in the line core. The ratio (Hα index) consequently measures any deviations, particularly emission, in the core. For detection efficiency, the shift of an emission feature relative to the central wavelength plays a significant role. Therefore, to come up with an optimum solution, we tried several configurations and finally settled upon a solution with filters (represented as a Gaussian function) centered on 655.5 nm with full width at half maxima of 12.5 and 3.5 nm, respectively. The filter curves and two example spectra are shown in Fig. 2, which also illustrates a classical P Cygni profile with the corresponding radial velocity shifts.

The final diagnostic diagram was constructed using $(g_1 - y)$ magnitudes and is shown in Figure 3, which presents the results for the sample of normal stars and the sample of classical Be and Herbig Ae/Be stars. In general, we assume that any object with Hα index < 3.35 over the full colour (effective temperature) range shows emission in the Hα line. This is a quite strict criterion that selects 711 (90%) of the 794 sample objects.

4. Conclusions

Our results show that synthetic photometry of the 520 nm and Hα region is an efficient tool for finding hot emission-line objects and that *Gaia* BP/RP spectra are excellently suited for this purpose. The well-established tool of Δa photometry covered the bluer spectral range, for which photoelectric measurements are also available. To probe the Hα region, we employed a wide and a narrow filter and calculated the ratio of the fluxes in both filters.

We analyzed the behavior of a sample of classical Be and Herbig Ae/Be stars and a control sample of normal stars in the corresponding colour-colour diagrams. About 90% of the emission-type objects could be unambiguously retrieved in this way. The method employed here can, therefore, be used as a blueprint in future studies to efficiently search for emission-line objects in *Gaia* BP/RP spectra.

References

Abdurro'uf, Accetta, K., Aerts, C., et al., The Seventeenth Data Release of the Sloan Digital Sky Surveys: Complete Release of MaNGA, MaStar, and APOGEE-2 Data. 2022, *Astrophysical Journal, Supplement*, **259**, 35, DOI: 10.3847/1538-4365/ac4414

Anusha, R., Mathew, B., Shridharan, B., et al., Identification of new classical Ae stars in the Galaxy using LAMOST DR5. 2021, *Monthly Notices of the RAS*, **501**, 5927, DOI: 10.1093/mnras/staa3964

Babusiaux, C., Fabricius, C., Khanna, S., et al., Gaia Data Release 3: Catalogue Validation. 2022, *arXiv e-prints*, arXiv:2206.05989

Bernhard, K., Otero, S., Hümmerich, S., et al., An investigation of the photometric variability of confirmed and candidate Galactic Be stars using ASAS-3 data. 2018, *Monthly Notices of the RAS*, **479**, 2909, DOI: 10.1093/mnras/sty1320

Blanton, M. R., Bershady, M. A., Abolfathi, B., et al., Sloan Digital Sky Survey IV: Mapping the Milky Way, Nearby Galaxies, and the Distant Universe. 2017, *Astronomical Journal*, **154**, 28, DOI: 10.3847/1538-3881/aa7567

Carrasco, J. M., Weiler, M., Jordi, C., et al., Internal calibration of Gaia BP/RP low-resolution spectra. 2021, *Astronomy and Astrophysics*, **652**, A86, DOI: 10.1051/0004-6361/202141249

Catanzaro, G., Spectroscopic atlas of Hα and Hβ in a sample of northern Be stars. 2013, *Astronomy and Astrophysics*, **550**, A79, DOI: 10.1051/0004-6361/201220357

Collins, George W., I., The Use of Terms and Definitions in the Study of be Stars (review Paper). 1987, in *IAU Colloq. 92: Physics of Be Stars*, ed. A. Slettebak & T. P. Snow, 3

Cui, X.-Q., Zhao, Y.-H., Chu, Y.-Q., et al., The Large Sky Area Multi-Object Fiber Spectroscopic Telescope (LAMOST). 2012, *Research in Astronomy and Astrophysics*, **12**, 1197

De Angeli, F., Weiler, M., Montegriffo, P., et al., Gaia Data Release 3: Processing and validation of BP/RP low-resolution spectral data. 2022, *arXiv e-prints*, arXiv:2206.06143, DOI: 10.48550/arXiv.2206.06143

Gaia Collaboration, Prusti, T., de Bruijne, J. H. J., et al., The Gaia mission. 2016, *Astronomy and Astrophysics*, **595**, A1, DOI: 10.1051/0004-6361/201629272

Gaia Collaboration, Vallenari, A., Brown, A. G. A., et al., Gaia Data Release 3: Summary of the content and survey properties. 2022, *arXiv e-prints*, arXiv:2208.00211

Haemmerlé, L., Eggenberger, P., Ekström, S., et al., Stellar models and isochrones from low-mass to massive stars including pre-main sequence phase with accretion. 2019, *Astronomy and Astrophysics*, **624**, A137, DOI: 10.1051/0004-6361/201935051

Hanuschik, R. W., Hummel, W., Sutorius, E., Dietle, O., & Thimm, G., Atlas of high-resolution emission and shell lines in Be stars. Line profiles and short-term variability. 1996, *Astronomy and Astrophysics, Supplement*, **116**, 309

Jaschek, M. & Egret, D., Catalog of Be stars. in , *Be Stars*, ed. M. Jaschek & H. G. Groth, Vol. **98**, 261

Kodaira, K., Osawa's Peculiar Star HD 221568. 1969, *Astrophysical Journal, Letters*, **157**, L59, DOI: 10.1086/180385

Kurfürst, P., Feldmeier, A., & Krtička, J., Two-dimensional modeling of density and thermal structure of dense circumstellar outflowing disks. 2018, *Astronomy and Astrophysics*, **613**, A75, DOI: 10.1051/0004-6361/201731300

Labadie-Bartz, J., Pepper, J., McSwain, M. V., et al., Photometric Variability of the Be Star Population. 2017, *Astronomical Journal*, **153**, 252, DOI: 10.3847/1538-3881/aa6396

Paunzen, E. & Prišegen, M., The detection of magnetic chemically peculiar stars using Gaia BP/RP spectra. 2022, *Astronomy and Astrophysics*, **667**, L10, DOI: 10.1051/0004-6361/202244839

Paunzen, E., Stütz, C., & Maitzen, H. M., On the detection of chemically peculiar stars using Δa photometry. 2005, *Astronomy and Astrophysics*, **441**, 631, DOI: 10.1051/0004-6361:20053001

Pavlovski, K. & Maitzen, H. M., Delta-a-photometry of Be shell stars. 1989, *Astronomy and Astrophysics, Supplement*, **77**, 351

Porter, J. M. & Rivinius, T., Classical Be Stars. 2003, *Publications of the ASP*, **115**, 1153, DOI: 10.1086/378307

Rivinius, T., Baade, D., & Štefl, S., Non-radially pulsating Be stars. 2003, *Astronomy and Astrophysics*, **411**, 229, DOI: 10.1051/0004-6361:20031285

Rivinius, T., Carciofi, A. C., & Martayan, C., Classical Be stars. Rapidly rotating B stars with viscous Keplerian decretion disks. 2013, *Astronomy and Astrophysics Reviews*, **21**, 69, DOI: 10.1007/s00159-013-0069-0

Shridharan, B., Mathew, B., Nidhi, S., et al., Discovery of 2716 hot emission-line stars from LAMOST DR5. 2021, *Research in Astronomy and Astrophysics*, **21**, 288, DOI: 10.1088/1674-4527/21/11/288

Skrutskie, M. F., Cutri, R. M., Stiening, R., et al., The Two Micron All Sky Survey (2MASS). 2006, *Astronomical Journal*, **131**, 1163, DOI: 10.1086/498708

Slettebak, A., The Be Stars. 1979, *Space Science Reviews*, **23**, 541, DOI: 10.1007/BF00212356

Stigler, C., Maitzen, H. M., Paunzen, E., & Netopil, M., Spectrophotometric analysis of the 5200 Å region for peculiar and normal stars. 2014, *Astronomy and Astrophysics*, **562**, A65, DOI: 10.1051/0004-6361/201322300

Strömgren, B., Spectral Classification Through Photoelectric Narrow-Band Photometry. 1966, *Annual Review of Astron and Astrophys*, **4**, 433, DOI: 10.1146/annurev.aa.04.090166.002245

Vioque, M., Oudmaijer, R. D., Schreiner, M., et al., Catalogue of new Herbig Ae/Be and classical Be stars. A machine learning approach to Gaia DR2. 2020, *Astronomy and Astrophysics*, **638**, A21, DOI: 10.1051/0004-6361/202037731

Zhang, Y.-J., Hou, W., Luo, A. L., et al., A Catalog of Early-type Hα Emission-line Stars and 62 Newly Confirmed Herbig Ae/Be Stars from LAMOST Data Release 7. 2022, *Astrophysical Journal, Supplement*, **259**, 38, DOI: 10.3847/1538-4365/ac4964

Zhao, G., Zhao, Y.-H., Chu, Y.-Q., Jing, Y.-P., & Deng, L.-C., LAMOST spectral survey — An overview. 2012, *Research in Astronomy and Astrophysics*, **12**, 723

The theory of hot white dwarfs of small and intermediate masses within the hybrid model

M. Vavrukh[ID] and D. Dzikovskyi[ID]

*Department of Astrophysics, Ivan Franko National University, Kyrylo &
Methodiy str. 8, 79005 Lviv, Ukraine, (E-mail: mvavrukh@gmail.com)*

Abstract. A new equation of state for hot white dwarfs of small and interme-
diate masses, which takes into account the contribution of an ideal relativistic
electron subsystem, the contribution of a gas nuclear subsystem, and the light
pressure was proposed. The internal structure of dwarfs was calculated within
such model. It was shown that the proposed model agrees with the observed
distribution of white dwarfs on the mass-radius plane. Based on the observed
data on masses and radii of white dwarfs, there was solved the inverse problem
– the determination of model parameters for the specific stars.

Key words: methods: analytical – stars: white dwarfs – stars: fundamental
parameters – stars: interiors

1. Introduction

The discovery of white dwarfs at the beginning of the last century (Adams,
1915) gave a rise to the problem of energy sources and stability of stars, which
have no thermonuclear reactions or occur only in the outer layers with a low
intensity and therefore play a secondary role. According to the idea of Fowler
(1926), the stability of white dwarfs is provided by the quantum effect – the
degeneracy of the electron subsystem, when $k_B T$ is much smaller than the elec-
tron energy at the Fermi surface. Chandrasekhar generalized this idea to the
case of high densities, for which the electron subsystem is relativistic, and con-
structed the theory of cold white dwarfs based on the hydrostatic equilibrium
equation (Chandrasekhar, 1931). The Chandrasekhar model is two-component:
a completely degenerate ideal electron subsystem and a subsystem of nuclei,
which is considered as a continuous classical environment. The equilibrium
between the pressure of electron gas at $T = 0\,K$ and the gravitational com-
pression, created by the nuclear subsystem provides the stability of a white
dwarf. The white dwarf characteristics (mass, radius, and distribution of mat-
ter) are functions of two dimensionless parameters: the relativistic parameter
$x_0 = \hbar(m_e c)^{-1}(3\pi^2 n(0))^{1/3}$ ($n(0)$ is the number density of electrons in the stel-
lar center, m_e is the electron mass, c is the speed of light) and the chemical
composition parameter $\mu_e = \langle A/z \rangle \approx 2.0$, where A is the mass number, z is the

charge of the nucleus. The main conclusions from Chandrasekhar's theory are the peculiar unambiguous mass-radius dependence and the restriction on the maximal mass (the Chandrasekhar limit),

$$M_{\max} = 2.01824\ldots\mu_e^{-2}M_0,$$
$$M_0 = \left(\frac{3}{2}\right)^{1/2}\frac{1}{4\pi m_u^2}\left(\frac{hc}{G}\right)^{3/2} \approx 2.8866\ldots M_\odot, \tag{1}$$

where m_u is the atomic mass unit. The restriction on the mass is confirmed by observations: for 110 years white dwarfs with masses $M > M_{\max}$ have not been detected. However, the mass-radius relation is satisfied only for white dwarfs of quite large masses ($M_{\max} > M \gtrsim 0.2M_0$) with small radii,

$$R \lesssim R_0 = \left(\frac{3}{2}\right)^{1/2}\frac{1}{4\pi m_u m_e}\left(\frac{h^3}{cG}\right)^{1/2} \approx 1.1\cdot 10^{-2}R_\odot. \tag{2}$$

This is clearly illustrated in Fig. 1a, constructed from the data of masses and radii of the observed white dwarfs from the catalog of Tremblay et al. (2011). The envelope dashed curve in Fig. 1b corresponds to the Chandrasekhar theory. The chains in Fig. 1b correspond to the observed white dwarfs with the same effective temperature, from which follow the conclusion about the important role of the finite temperature effects in the formation of white dwarfs' characteristics with small and intermediate masses. The problem of the internal structure of hot white dwarfs of small masses became relevant only after a wide variety of the characteristics of white dwarfs (masses, radii, effective temperatures, and luminosities) were revealed during the last 25 years with the help of space observatories. The Chandrasekhar model uses the equation of state of a completely degenerate ideal electron subsystem. From a modern view point, it is quite idealized and does not take into account the important factors of the white dwarfs' structure formation: interparticle interactions, axial rotation, magnetic fields and finite temperature effects. This is the basic model that explains the existence and stability of massive cold white dwarfs. It cannot explain the radiation of white dwarfs and the main details of their distribution on the mass-radius plane. Hot low-mass white dwarfs should not be considered correctly within the Chandrasekhar model, because their effective temperature reaches $(4\div 8)\cdot 10^4\,K$, and the luminosity of some of them exceeds the luminosity of the Sun.

The problem of energy sources of white dwarfs was actively discussed in 1939-1952. Marshak (1940) followed the idea of gravitational compression, but did not investigate this mechanism. Schatzman proposed the idea of thermonuclear reactions in the surface layers of white dwarfs. A physically based idea, according to which white dwarfs emit a reserve of thermal energy accumulated in the past due to thermonuclear reactions, was proposed by Kaplan (1949, 1950). According to his idea, thermal energy is mainly concentrated in the nuclear subsystem, which can be considered as a classical ideal gas. The average value
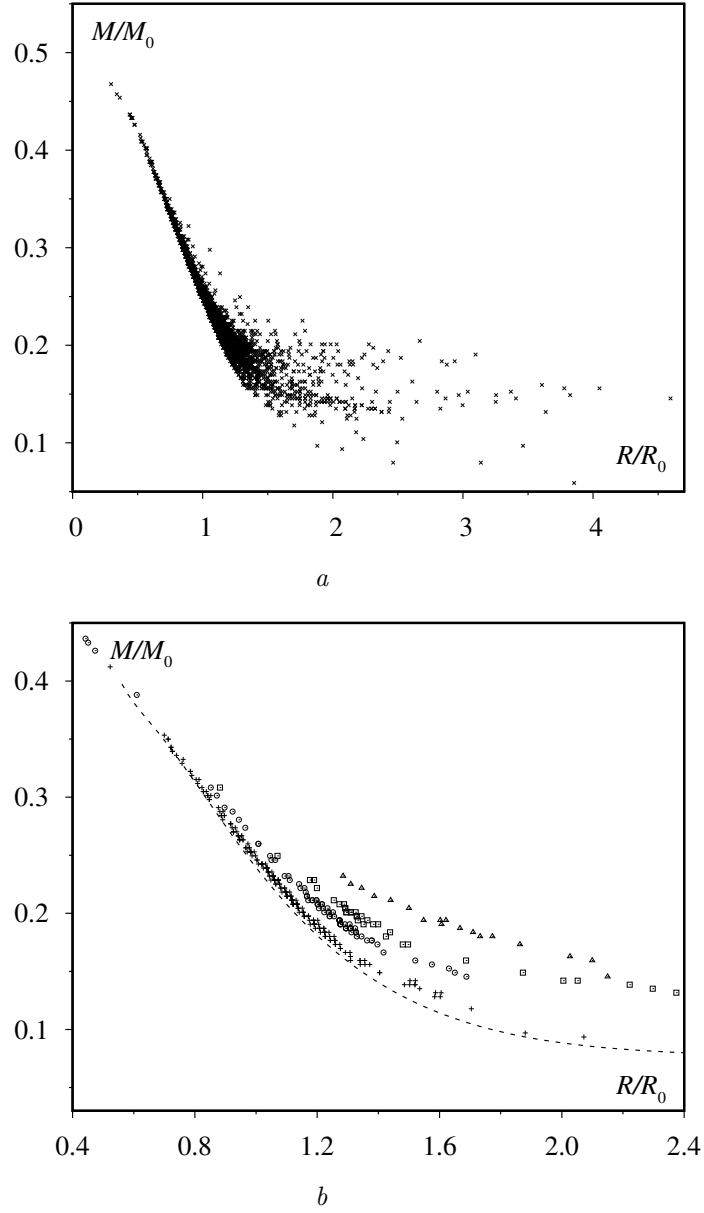
Figure 1. The coordinates of white dwarfs of the spectral class DA with different temperatures on the mass-radius plane (data about masses and radii are taken from the catalog of Tremblay et al. (2011)). The chains correspond to the white dwarfs with close values of effective temperatures. The dashed curve is the mass-radius dependence for the cold white dwarfs.

of the kinetic energy of such model is

$$W_T \approx \frac{3}{2} \frac{k_B}{m_u \mu_n} \int_V \rho(\mathbf{r}) T(\mathbf{r}) d\mathbf{r} \approx \frac{3}{2} \frac{k_B}{m_u \mu_n} MT, \tag{3}$$

where $\rho(\mathbf{r})$ is the density of matter, μ_n is the dimensionless molecular mass of the nucleus in the units m_u, $T \equiv \langle T(\mathbf{r}) \rangle$ is the average value of temperature by the stellar volume. We can estimate the temperature value in the inner part of a white dwarf (which is considered nearly isothermal due to the electron mechanism of heat conduction) by the Schatzman (1947) formula

$$T = T_0 \left(\frac{L/L_\odot}{M/M_\odot} \right)^{2/7}, \quad T_0 = 6.16 \cdot 10^7 \, K. \tag{4}$$

This expression is obtained by analyzing the system of structural equations in the peripheral region of a white dwarf (Shapiro & Teukolsky, 1983). According to Kaplan's idea, the luminosity is

$$L \approx -\frac{d}{dt} W_T \approx -\frac{3}{2} \frac{k_B}{m_u \mu_n} M \frac{dT}{dt}. \tag{5}$$

On the other hand, the luminosity can be determined from equation (4),

$$L = L_\odot \frac{M}{M_\odot} \left(\frac{T}{T_0} \right)^{7/2}. \tag{6}$$

Equating the right-hand sides of equalities (5) and (6), Kaplan obtained a differential equation that determines the dependence of the white dwarf's temperature on its age, or cooling time of a white dwarf (Kaplan, 1950)

$$\tau = \tau_0 \left(\frac{M/M_\odot}{L/L_\odot} \right)^{5/7}, \quad \tau_0 = \frac{3}{5} \frac{k_B T_0}{m_u \mu_n} \frac{M_\odot}{L_\odot} \approx \frac{5}{\mu_n} \cdot 10^7 \, \text{years}. \tag{7}$$

At the same time, it is assumed that the temperature of the white dwarf at the time of its formation was much higher than observed at the present time. For low-luminosity white dwarfs $L/L_\odot \approx 10^{-5}$, therefore the cooling time is of the order of 10^9 years. For hot white dwarfs with masses $M \approx 0.2 M_0$ and effective temperatures $T_{\text{eff}} \approx 5 \cdot 10^4 \, K$ the luminosity $L \approx L_\odot$, therefore the cooling time for them is close to 10^7 years. For bright white dwarfs of small masses with temperatures $T_{\text{eff}} \approx (7 \div 9) \cdot 10^4 \, K$, the cooling time is of the order of $3 \cdot 10^6$ years.

In Tab. 1 there are shown the data of masses, radii and luminosities of low-mass dwarfs with effective temperatures in the range $(2 \div 9) \cdot 10^4 \, K$. In this Table there are also shown the estimates of an average dimensionless temperature $T_* = k_B T / m_e c^2$ according to formula (4).

Table 1. The macroscopic characteristics of DA type white dwarfs from the catalog of Tremblay et al. (2011).

Number	R/R_0	M/M_0	T_{eff}, K	T_*
3	1.8295	0.145498	23010	0.00669
111	1.91470	0.142034	25740	0.00787
104	2.3415	0.176676	72130	0.02692
106	2.87548	0.180140	84430	0.03605
158	3.82335	0.148962	78960	0.04149
266	1.74757	0.152426	28480	0.00821
377	2.11256	0.128177	20890	0.00671
688	1.95930	0.142034	27970	0.00876
592	2.42551	0.193997	86620	0.03297
921	1.29941	0.232104	54370	0.01288
928	2.27731	0.200926	88080	0.03209
2472	1.28454	0.232104	51770	0.01209
2531	1.34523	0.221711	50170	0.01213
2836	0.89115	0.322174	58380	0.01025
2929	1.24836	0.245961	60420	0.01397
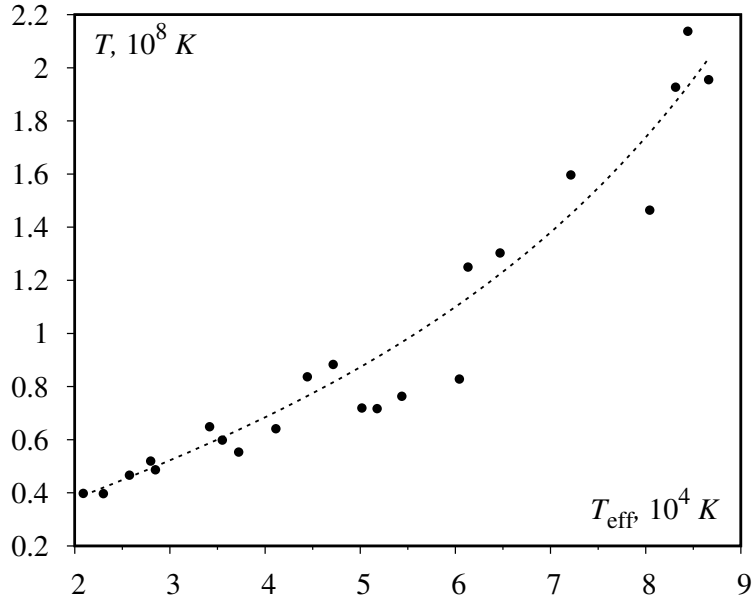
Figure 2. Dependence of the temperature T on the effective temperature T_{eff}, calculated by formula (4) for the group of white dwarfs from the catalog of Tremblay et al. (2011).

It should be expected that due to the high thermal conductivity of white dwarfs, the temperature in the inner region is higher, the higher effective temperature. This is confirmed by Fig. 2, which shows the dependence "$T_{\text{eff}} - T$", where T_{eff} is taken from the catalog of Tremblay et al. (2011), and T is calculated by formula (4). It would be incorrect to neglect the pressure of the nuclear subsystem at such high temperatures.

To clarify the elementary theory of cooling of white dwarfs as described above, we used a model in which the structure of the nuclear subsystem can vary from an ideal gas to a crystal lattice (Shapiro & Teukolsky, 1983). At the same time, the role of the electron subsystem was not taken into account, as in the work of Kaplan (1950).

Further development of this approach for the calculation of massive white dwarfs can be found in the work of Bisnovatyi-Kogan (1966), in which the temperature correction ($\sim T^2$) to the pressure of the electron subsystem is taken into account within the isothermal electron-nuclear model.

2. Model and equation of state

As it was shown from the calculation supplementing the Chandrasekhar model by the axial rotation (James, 1964) or interparticle interactions (Vavrukh et al., 2018), these have a little effect on the characteristics of cold massive dwarfs. High effective temperatures and observed distribution on the mass-radius plane indicate the important role of the finite temperature effects in the formation of hot white dwarfs structure. This is confirmed by approximate calculations within the generalized Chandrasekhar model, in which the electron subsystem is not completely degenerate (Vavrukh & Smerechynskyi, 2012, 2013).

The purpose of our work is to calculate the internal structure of specific observed white dwarfs within a simple spherically symmetric two-component model: a partially degenerate ideal electron subsystem + a nuclear subsystem which is considered as an ideal classical gas. Such model corresponds to the equation of state

$$P(\mathbf{r}) = P_e(\mathbf{r}) + P_n(\mathbf{r}) + P_{\text{ph}}(\mathbf{r}). \tag{8}$$

where $P_e(\mathbf{r})$ is the partial pressure of the electron subsystem on the sphere of radius r,

$$P_n(\mathbf{r}) = \frac{k_B T(\mathbf{r})}{m_u \mu_n} \rho(\mathbf{r}) \tag{9}$$

is the partial pressure of the nuclear subsystem, where $T(\mathbf{r})$ is the local temperature and $\rho(\mathbf{r})$ is the density of matter. The term

$$P_{\text{ph}}(\mathbf{r}) = \frac{a}{3} T^4(\mathbf{r}) \tag{10}$$

takes into account the photon pressure ($a = k_B^4 (\hbar c)^{-3} \pi^2 / 15$). The correct description of the electron subsystem of a hot white dwarf requires the usage

of two-phase or three-phase models: because in the inner region the electron subsystem is relativistic and deviation from the total degeneracy is small; in the periphery region the subsystem is degenerate, but not relativistic; near the star surface electrons can be considered as an ideal classical gas (Vavrukh & Smerechynskyi, 2012). However, the contributions of the peripheral region to the integral characteristics are small due to the low density. Therefore, to simplify the problem, we will assume that the electron gas is everywhere degenerate, and its chemical potential μ is positive. The terms $P_e(\mathbf{r})$ and $P_n(\mathbf{r})$ depend on the thermodynamic parameters $\rho(\mathbf{r})$ and $T(\mathbf{r})$. In order to simplify the problem, we will pass to one parameter – the local relativistic parameter

$$x(\mathbf{r}) = \frac{\hbar}{m_e c} \left[3\pi^2 n(\mathbf{r}) \right]^{1/3}, \tag{11}$$

where $n(\mathbf{r})$ is the number density of electrons on the sphere of radius r, and therefore the density of matter

$$\rho(\mathbf{r}) = \frac{m_u \mu_e}{3\pi^2} \left(\frac{m_e c}{\hbar} \right)^3 x^3(\mathbf{r}). \tag{12}$$

According to the method of Eddington (1926), the sum of light pressure and gas pressure of the nuclear subsystem can be approximately represented in the form of a polytropic dependence

$$P_{\mathrm{ph}}(\mathbf{r}) + P_n(\mathbf{r}) = K[\rho(\mathbf{r})]^{4/3}, \quad K = \left[\frac{1-\beta}{\beta^4} \right]^{1/3} \frac{\hbar c}{(m_u \mu_n)^{4/3}} \left(\frac{45}{\pi^2} \right)^{1/3}, \tag{13}$$

where the coefficient β determines the relative value of gas pressure ($\beta = P_n(\mathbf{r})[P_n(\mathbf{r}) + P_{\mathrm{ph}}(\mathbf{r})]^{-1} = const$). Relations (9) – (13) determine the dependence between the matter density and temperature,

$$k_B T(\mathbf{r}) = \gamma \frac{\hbar c}{(m_u \mu_n)^{1/3}} \rho^{1/3}(\mathbf{r}) = \gamma \left(\frac{\mu_e}{\mu_n} \right)^{1/3} (3\pi^2)^{-1/3} m_e c^2 x(\mathbf{r}), \tag{14}$$

and the coefficient γ is the root of the equation

$$\frac{\pi^2}{45} \gamma^4 + \gamma = \alpha, \quad \alpha \equiv K(\hbar c)^{-1} (m_u \mu_n)^{4/3}. \tag{15}$$

According to relations (12) – (14)

$$P_n(\mathbf{r}) + P_{\mathrm{ph}}(\mathbf{r}) = \frac{\pi m_e^4 c^5}{3h^3} \frac{8\alpha}{(3\pi^2)^{1/3}} \left(\frac{\mu_e}{\mu_n} \right)^{4/3} x^4(\mathbf{r}). \tag{16}$$

As it was known (Shapiro & Teukolsky, 1983), the equation of state of an ideal homogeneous relativistic subsystem of electrons at finite temperatures is written

in the following parametric form

$$
\begin{cases}
P_e = \dfrac{8\pi}{3h^3} \int\limits_0^\infty dp\, p^3 \dfrac{dE_p}{dp}\, n_p, \\[2mm]
\dfrac{N_e}{V} = \dfrac{8\pi}{h^3} \int\limits_0^\infty dp\, p^2\, n_p,
\end{cases}
\tag{17}
$$

where

$$
E_p = [(m_e c^2)^2 + p^2 c^2]^{1/2} - m_e c^2, \;\; n_p = \left\{ 1 + \exp[(E_p - \mu)/k_B T] \right\}^{-1}. \tag{18}
$$

The deviation from the absolute degeneracy can be considered small if $\mu(k_B T)^{-1} \gg 1$. The approximate calculations of integrals (17) at this basis and the following exception μ from the obtained system of algebraic equations allows us to represent P_e as follows

$$
\begin{aligned}
P_e(x) &= \frac{\pi m_e^4 c^5}{3h^3} \left\{ \mathcal{F}_0(x) + \mathcal{F}_2(x) + \mathcal{F}_4(x) + \cdots \right\}, \\
\mathcal{F}_0(x) &= x(2x^2 - 3)(1 + x^2)^{1/2} + 3\ln[x + (1 + x^2)^{1/2}]; \\
\mathcal{F}_2(x) &= \frac{4\pi^2 T_*^2}{3} \frac{x(2 + x^2)}{(1 + x^2)^{1/2}}; \\
\mathcal{F}_4(x) &= -\frac{\pi^4}{45} T_*^4 \left[72 + 136x^2 + 77x^4 + 18x^6 \right] x^{-3}(1 + x^2)^{-3/2}; \dots.
\end{aligned}
\tag{19}
$$

Here $\mathcal{F}_0(x)$ determines the pressure of the absolute degenerate electron subsystem (at $T = 0$) and has the following asymptotics

$$
\mathcal{F}_0(x) \to
\begin{cases}
2x^4 - 2x^2 + \cdots & \text{at } x \gg 1, \\[2mm]
\dfrac{8}{5}x^5 - \dfrac{4}{7}x^7 + \cdots & \text{at } x \ll 1.
\end{cases}
\tag{20}
$$

The dimensionless temperature is determined by the relation

$$
T_* = k_B T (m_e c^2)^{-1}. \tag{21}
$$

To obtain the coordinate dependence of the partial pressure of the electron subsystem in the white dwarfs' model, x should be replaced in formulae (19) and (20) by the local value of the relativistic parameter (11).

To simplify the problem, we model the coordinate dependence of temperature in expressions (19). The significant deviation from the absolute degeneracy of the electron subsystem occurs when $k_B T(r)$ is proportional to the local value of the Fermi energy,

$$
k_B T(r) \approx A \cdot m_e c^2 \left\{ [1 + x^2(r)]^{1/2} - 1 \right\}. \tag{22}
$$

We select the coefficient A so that for $x(r) \gg 1$ the relation between $T(r)$ and $x(r)$ is given by expression (14). At this condition

$$T_*(r) \approx \alpha(3\pi^2)^{-1/3} \left(\frac{\mu_e}{\mu_n}\right)^{1/3} \left\{(1 + x^2(r))^{1/2} - 1\right\}. \tag{23}$$

At this modeling of the coordinate dependence of the dimensionless temperature, all terms $\mathcal{F}_2(x(r))$, $\mathcal{F}_4(x(r))$, ... have the same asymptotics relative to the $x(r)$ as the main term of expansion (see (20)), temperature corrections are small and series (19) coincides. At this $\mathcal{F}_2(x(r)) \sim \alpha^2$, $\mathcal{F}_4(x(r)) \sim \alpha^4$ and etc. We restrict ourselves to the quadratic approximation by $T_*(r)$, which makes it possible to depict the model equation of state in the following approximate form

$$P(\mathbf{r}) \cong \frac{\pi m_e^4 c^5}{3h^3} \left\{ \mathcal{F}_0(x(\mathbf{r})) + \frac{8\alpha}{(3\pi^2)^{1/3}} \left(\frac{\mu_e}{\mu_n}\right)^{4/3} x^4(\mathbf{r}) + \right.$$
$$\left. + 4\alpha^2 \pi^{2/3} 3^{-5/3} \left(\frac{\mu_e}{\mu_n}\right)^{2/3} f(x(\mathbf{r})) \right\}, \tag{24}$$

where

$$f(x(\mathbf{r})) = x(\mathbf{r})[2 + x^2(\mathbf{r})](1 + x^2(\mathbf{r}))^{-1/2} \left\{[1 + x^2(\mathbf{r})]^{1/2} - 1\right\}^2, \tag{25}$$

and α is the model parameter. Due to the presence of multiplier α^2, the third term in the curly bracket of formula (24) is small, which allows us to take it into account by the approximate method. As it is easy to see, the ratio $f(x)/\mathcal{F}_0(x)$ in the interval $0 \leq x \leq 1$ is a monotonously decreasing function that very weakly depends on x and varies from the value 0.3125 at $x = 0$ to the value 0.2959 at $x = 1$. Therefore, the sum of the first and third terms in the curly bracket of formula (24) with sufficiently high accuracy can be written in the form

$$\mathcal{F}_0(x(\mathbf{r})) \left\{ 1 + 1.216\alpha^2 \pi^{2/3} 3^{-5/3} \left(\frac{\mu_e}{\mu_n}\right)^{2/3} \right\} \equiv \mathcal{F}_0(x(\mathbf{r}))(1 + B), \tag{26}$$

replacing the fraction $f(x)/\mathcal{F}_0(x)$ with its average value 0.304 on the interval $0 \leq x \leq 1$. Here

$$B = 1.216\alpha^2 \pi^{2/3} 3^{-5/3} \left(\frac{\mu_e}{\mu_n}\right)^{2/3}. \tag{27}$$

3. Equilibrium equation

The internal structure of a white dwarf is determined by the equilibrium equation

$$\nabla P(\mathbf{r}) = -\rho(\mathbf{r})\nabla \Phi(\mathbf{r}), \tag{28}$$

where

$$\Phi(\mathbf{r}) = -G \int\limits_V \frac{\rho(\mathbf{r}')d\mathbf{r}'}{|\mathbf{r} - \mathbf{r}'|} \tag{29}$$

is the gravitational potential on the sphere of radius r, created by the distribution of matter. Using equation of state (24) in approximation (26) and relation (12), let us reduce equation (28) to

$$(1 + B)\frac{x(\mathbf{r})\nabla x(\mathbf{r})}{[1 + x^2(\mathbf{r})]^{1/2}} + C\nabla x(\mathbf{r}) = -\frac{m_u\mu_e}{m_e c^2}\,\nabla\Phi(\mathbf{r}), \tag{30}$$

where

$$C = \frac{4\alpha}{(3\pi^2)^{1/3}}\left(\frac{\mu_e}{\mu_n}\right)^{4/3}. \tag{31}$$

Using the identity

$$\frac{x\nabla x}{[1 + x^2]^{1/2}} = \nabla\big\{[1 + x^2]^{1/2} - 1\big\}, \tag{32}$$

acting by operator ∇ on equation (30) and taking into account that $\nabla^2\Phi(\mathbf{r}) = 4\pi G\rho(\mathbf{r})$, we obtain the differential equation for the local value of the relativistic parameter

$$(1 + B)\Delta\big\{[1 + x^2(\mathbf{r})]^{1/2} - 1 + \tilde{C}x(\mathbf{r})\big\} = -\frac{32\pi^2 G}{3(hc)^3}\left[m_e m_u \mu_e c^2\right]^2 x^3(\mathbf{r}), \tag{33}$$

where $\tilde{C} = C/(1 + B)$. It follows from formulae (27) and (31) that $B = 1.216\,C^2\pi^2(48)^{-1}(\mu_n/\mu_e)^2$, and $\tilde{C} = C\{1 + 1.216\,C^2\pi^2(48)^{-1}(\mu_n/\mu_e)^2\}^{-1}$. We consider a white dwarf without axial rotation i. e. beings spherically symmetric, and its chemical composition is spatially homogeneous. Therefore, in our model there appear four dimensionless parameters: $x_0 \equiv x(0)$ (the relativistic parameter in the stellar center), C, μ_e and μ_n which for the specific white dwarf are constants.

In order to numerically solve the equilibrium equation, it is convenient to pass from the variables $(r, x(r))$ to the dimensionless variables

$$\xi = \frac{r}{\lambda}, \quad y(\xi) = \varepsilon_0^{-1}\big\{[1 + x^2(r)]^{1/2} - 1 + \tilde{C}x(r)\big\}, \tag{34}$$
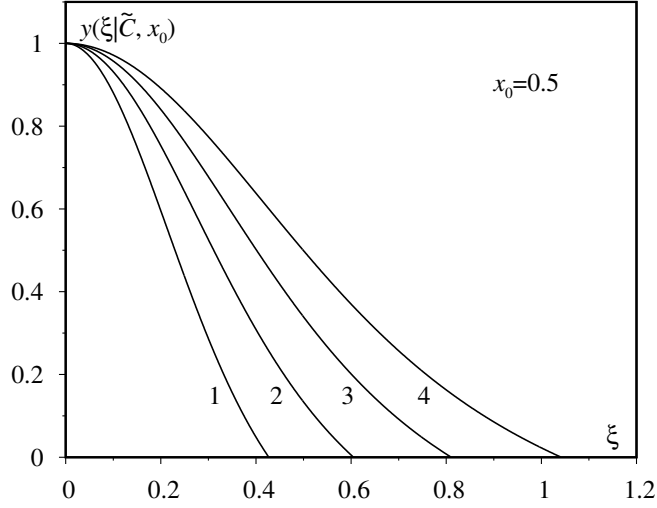
where

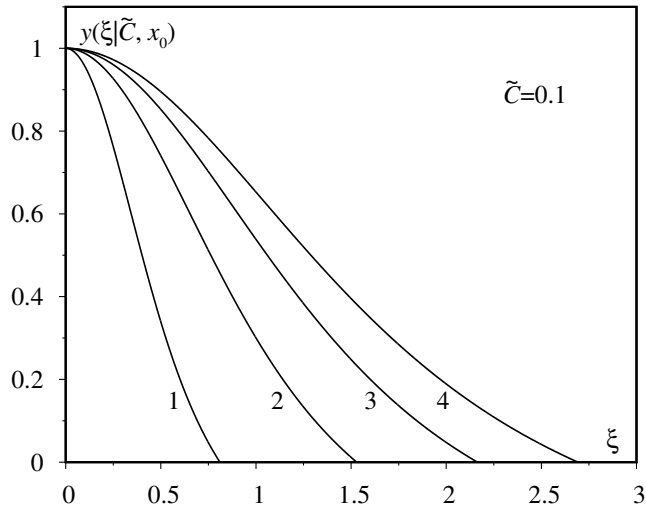$$\varepsilon_0 = \varepsilon_0(x_0, \tilde{C}) = (1 + x_0^2)^{1/2} - 1 + \tilde{C}x_0, \tag{35}$$

and λ is the length scale. If we determine it from the condition

$$\frac{32\pi^2 G}{3(hc)^3}\left\{m_e m_u \mu_e c^2 \lambda\varepsilon_0\right\}^2 = 1 + B \cong 1 + 1.216\,\frac{\pi^2}{48}\tilde{C}^2\left(\frac{\mu_n}{\mu_e}\right)^2, \tag{36}$$

Figure 3. The solution of the equilibrium equation at the fixed value of $x_0 = 0.5$ for different values of the parameter $\tilde{C}$. Curve 1 corresponds to the standard model at $\tilde{C} = 0$, curve 2 – $\tilde{C} = 0.05$, 3 – $\tilde{C} = 0.1$, 4 – $\tilde{C} = 0.15$.

Figure 4. The solution of the equilibrium equation at the fixed value of $\tilde{C} = 0.1$ for different values of the parameter x_0. Curve 1 corresponds to $x_0 = 0.5$, curve 2 – $x_0 = 1.0$, 3 – $x_0 = 1.5$, 4 – $x_0 = 2.0$.

and express $x(r)$ through $y(\xi)$ using definition (34), then the equation for the function $y(\xi)$ takes the form

$$\Delta_\xi y(\xi) = -x^3(\xi, \tilde{C}),$$

$$x(\xi, \tilde{C}) = \frac{x(r)}{\varepsilon_0} \equiv \left\{ \varepsilon_0(1 - \tilde{C}^2) \right\}^{-1} \left\{ [\tilde{C}^2 + (\varepsilon_0 y)^2 + 2\varepsilon_0 y]^{1/2} - \tilde{C}(1 + \varepsilon_0 y) \right\}. \tag{37}$$

This equation corresponds to the boundary condition $y(0) = 1$, as well the condition $dy/d\xi = 0$ at $\xi = 0$, which ensures the non-singular nature of the solution in the white dwarf center. As it is easy to see, in the limit $\tilde{C} \to 0$ the right-hand side of equation (37) equals $(y^2(\xi) + 2\varepsilon_{00}^{-1}y(\xi))^{3/2}$, as in the Chandrasekhar model, where $\varepsilon_{00} \equiv \varepsilon_0(x_0, 0)$. A set of solutions of the two-parametric equation (37), found by the numerical method for several values of parameters $\tilde{C}$ and x_0 is illustrated in Figs. 3 and 4.

In accordance with relations (34) the radius of the white dwarf is

$$R(x_0, \mu_e, \tilde{C}) = \lambda \xi_1(x_0, \tilde{C}) = R_0 \frac{\xi_1(x_0, \tilde{C})}{\mu_e \varepsilon_0(x_0, \tilde{C})} (1 + B)^{1/2}, \tag{38}$$

where $\xi_1(x_0, \tilde{C})$ is the root of equation $y(\xi | x_0, \tilde{C}) = 0$, and R_0 is determined by formula (2), $\lambda(C)$ is the root of equation (36), and parameters C and $\tilde{C}$ are related by

$$2\gamma C = \frac{1}{\tilde{C}} - \sqrt{\frac{1}{\tilde{C}^2} - 4\gamma}, \tag{39}$$

where $\gamma = \pi^2(48)^{-1}(\mu_n/\mu_e)^2$. The stellar mass is determined by the solution of equation (37),

$$M(x_0, \mu_e, \tilde{C}) = \frac{M_0}{\mu_e^2} \mathcal{M}(x_0, \tilde{C})(1 + B)^{3/2}, \tag{40}$$

where

$$\mathcal{M}(x_0, \tilde{C}) = \int_0^{\xi_1(x_0, \tilde{C})} \xi^2 x^3(\xi, \tilde{C}) \, d\xi. \tag{41}$$

Dependence of the dimensionless radius on the model parameters is illustrated in Fig. 5. Herewith, the dashed curve corresponds to the standard Chandrasekhar model ($\tilde{C} = 0$). The dimensionless white dwarf mass $\mathcal{M}(x_0, \tilde{C})$ is illustrated in Fig. 6 as a function of x_0 for different values of the parameter $\tilde{C}$. Relations (14) and (15) give us an opportunity to determine the temperature change along the radius

$$T(\xi, \tilde{C}) = \gamma \left(\frac{\mu_e}{\mu_n} \right)^{1/3} \frac{m_e c^2}{(3\pi^2)^{1/3} k_B} x(\xi, \tilde{C}). \tag{42}$$
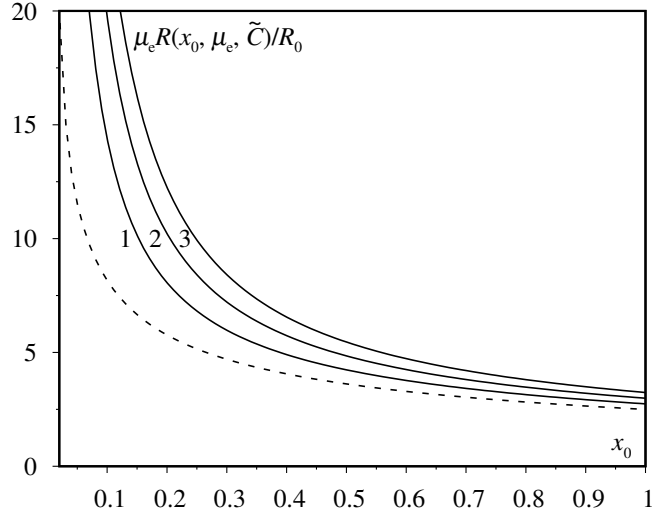
Figure 5. Dependence of the dimensionless radius on the relativistic parameter x_0 for different values of the parameter $\tilde{C}$. The dashed curve corresponds to the standard Chandrasekhar model with $\tilde{C} = 0$, curve $1 - \tilde{C} = 0.05$, $2 - \tilde{C} = 0.1$, $3 - \tilde{C} = 0.15$.
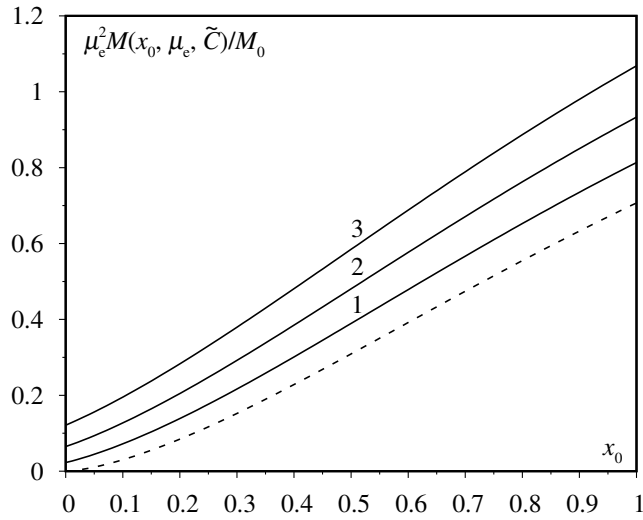
Figure 6. Dependence of the dimensionless mass $\mathcal{M}(x_0, \tilde{C})$ on the relativistic parameter x_0 for different values of the parameter $\tilde{C}$ (notations are the same as in the previous Figure).
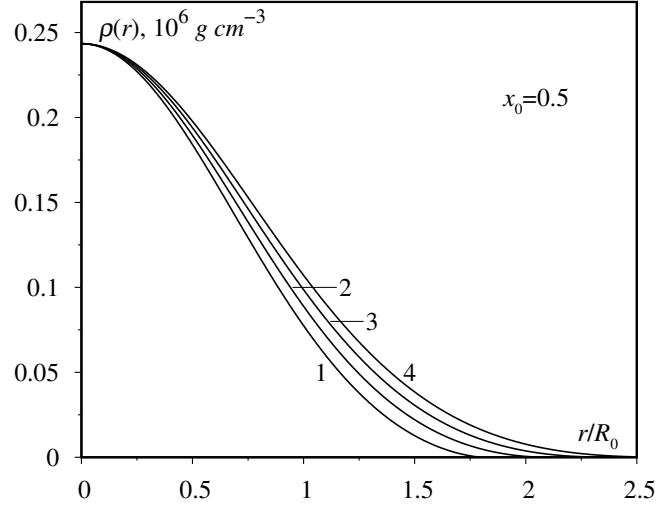
Figure 7. The distribution of matter density along the radius at the fixed value of $x_0 = 0.5$ for different values of the parameter $\tilde{C}$. Curve 1 corresponds to $\tilde{C} = 0$, 2 – $\tilde{C} = 0.05$, 3 – $\tilde{C} = 0.1$, 4 – $\tilde{C} = 0.15$.
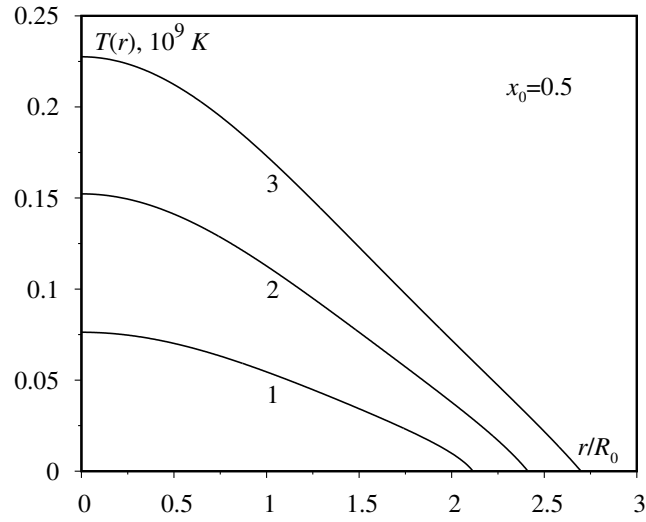

Figure 8. The distribution of temperature along the radius at the fixed value of $x_0 = 0.5$ for different values of the parameter $\tilde{C}$. Curve 1 corresponds to $\tilde{C} = 0.05$, 2– $\tilde{C} = 0.1$, 3 – $\tilde{C} = 0.15$.

To illustrate the capabilities of our approach in Figures 7 and 8 we show how both density and temperature vary with the radius.

The crosses in Fig. 9 depict the location of observed white dwarfs (from the catalog of Tremblay et al. (2011)) on the mass-radius plane. Curves in this figure depict the dependence between the mass and the radius of white dwarfs in our model. They were constructed from relations (38) – (41) for several values of the parameter $\tilde{C}$ for a range of the relativistic parameter ($0.3 \leq x_0 \leq 0.8$). Herewith, we used the value $\mu_e = 2$, as well as $\mu_n = 4$ (that corresponds to helium white dwarfs). As it is shown in Figure, in the selected region of the change of the parameter $\tilde{C}$ our model can describe the distribution of observed hot white dwarfs of small and intermediate masses on the mass-radius plane. This is impossible to achieve in the Chandrasekhar model, which corresponds to the lower curve in Figure with $\tilde{C} = 0$. The standard model satisfactorily describes only the distribution of white dwarfs with sufficiently large masses and radii $R(x_0, \tilde{C}) \lesssim R_0$.
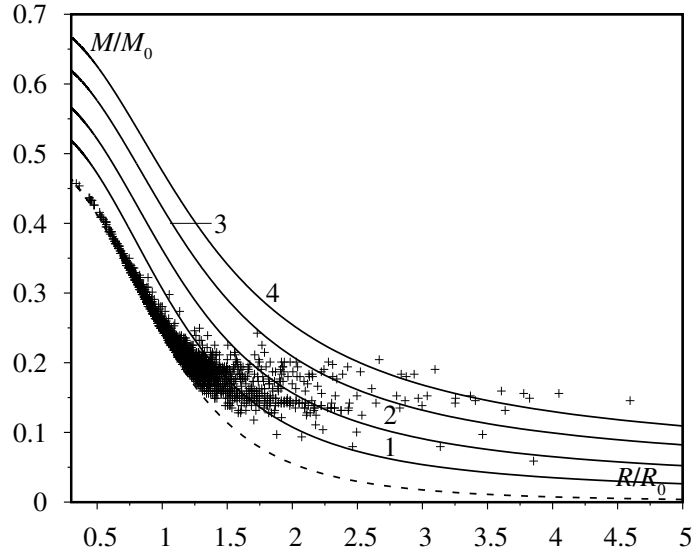
Figure 9. The mass-radius relation for different values of the parameter $\tilde{C}$. The dashed curve corresponds to the standard model ($\tilde{C} = 0$), curve $1 - \tilde{C} = 0.05$, $2 - \tilde{C} = 0.1$, $3 - \tilde{C} = 0.15$, $4 - \tilde{C} = 0.19$. The crosses correspond to the observed data from the catalog of Tremblay et al. (2011).

To calculate the internal structure of the observed white dwarfs, it is necessary first to solve the inverse problem of the theory – the determination of model parameters for a specific white dwarf based on the observed data. To

demonstrate the algorithm for such calculation, we consider Fig. 9 from which it can be seen that a theoretical mass-radius curve can always be drawn through a point with the given observed mass M and radius R with the certain parameter value $\tilde{C}$. This is the parameter value $\tilde{C}$ for a chosen white dwarf. Putting instead $R(x_0, \tilde{C})$ and $M(x_0, \tilde{C})$ the observed R and M in relations (38) and (40), we obtain the system of equations for the parameters x_0 and μ_e

$$
\begin{aligned}
\frac{R}{R_0} \frac{\varepsilon_0(x_0, \tilde{C})}{\xi_1(x_0, \tilde{C})} &= \frac{1}{\mu_e}(1+B)^{1/2}, \\
\frac{M}{M_0} &= \frac{1}{\mu_e^2} \mathcal{M}(x_0, \tilde{C})(1+B)^{3/2}.
\end{aligned}
\tag{43}
$$

Excluding μ_e, we obtain the equation

$$
\frac{M}{M_0} \left(\frac{R_0}{R} \right)^2 \left(\frac{\xi_1(x_0, \tilde{C})}{\varepsilon_0(x_0, \tilde{C})} \right)^2 = \mathcal{M}(x_0, \tilde{C})(1+B)^{1/2}
\tag{44}
$$

for finding the relativistic parameter x_0, after that the parameter μ_e is determined by the first of equations (43).

Since the parameter B plays the role of correction, it makes sense to consider a simplified version of the model with absolute degeneracy of the electron subsystem, that corresponds to $B = 0$ (or $\tilde{C} = C$). The model parameters for the group of white dwarfs from the catalog Tremblay et al. (2011) calculated in such way are shown in Tab. 2. Using relations (12) and (14), we calculated the density of matter and temperature in the center of these white dwarfs $\rho_c = \rho(0)$ and $T_c = T(0)$. These values are also shown in Tab. 2. As we can see, the temperature T_c^0 calculated by formula (4) is almost $(1.5 - 3)$ times smaller than the temperature T_c obtained by formula (42). This cannot be a criterion, because formula (4) is approximated and corresponds to the isothermal model.

In order to evaluate the role of incomplete degeneracy of the electron subsystem we considered a group of white dwarfs that corresponds to $C = 0.15$ in Tab. 2. At $B = 1.216\,(48)^{-1}\pi^2 C^2 (\mu_n/\mu_e)^2$ these dwarfs correspond to the mass-radius curve with $\tilde{C} = 0.142$. Model parameters x_0 and μ_e are determined from the system of equations (43), as well as calculated on this basis $\rho_c(0)$ and $T_c(0)$ are shown in Tab. 3. From the comparison of Tabs. 2 and 3 it follows that the influence of incomplete degeneracy of the electron subsystem is weak and leads to small changes of parameters and characteristics of the model. In particular, the relative decreasing of the relativistic parameter x_0 has an order of 0.6%, decreasing ρ_c corresponds to 2%, and the decreasing T_c is close to 5%.

4. Discussion

According to Fowler's idea, the stability of white dwarfs ensured by the pressure of the degenerate electron subsystem is an extrapolation of the real thermodynamical state of these objects in the case of low temperatures or high pressures.

Table 2. The characteristics and the model parameters for the group of white dwarfs of spectral class DA from the catalog Tremblay et al. (2011) at $B = 0$ (T_c^0 approximately corresponds to equation (4)).

Number	R/R_0	M/M_0	x_0	μ_e	ρ_c, 10^6 g cm^{-3}	T_c, 10^9 K	T_c^0, 10^9 K
			$C = 0.1$				
2270	3.13742	0.079677	0.346458	2.03348	0.080993	0.105513	0.048904
3026	2.09943	0.142034	0.603049	2.00554	0.427125	0.183657	0.069994
441	1.88942	0.166283	0.703784	1.99963	0.678915	0.214336	0.090419
2581	1.67358	0.197461	0.841388	1.99714	1.160080	0.256243	0.106619
			$C = 0.15$				
2922	2.82645	0.135105	0.472760	1.99620	0.205788	0.215153	0.144974
1246	2.64303	0.142034	0.508990	2.01176	0.256818	0.231642	0.146958
2606	2.49710	0.152426	0.548329	2.00757	0.321086	0.249545	0.141763
2090	2.15203	0.183604	0.668973	1.99890	0.583074	0.304450	0.148608
2507	1.98346	0.200926	0.744181	2.00258	0.802663	0.338677	0.157729
			$C = 0.19$				
2017	3.63580	0.131641	0.387910	1.99912	0.113682	0.222433	0.069164
397	3.25419	0.148962	0.444555	1.98260	0.171109	0.254914	0.211635
592	2.42551	0.193997	0.626813	1.99922	0.479636	0.359423	0.199981

Chandrasekhar's theory is based on this idea. The position of observed white dwarfs on the mass-radius plane indicates the different ages of these stars and reflects their evolution. The generalized theory of white dwarfs can be built by generalization of Fowler's idea, using a more general form of the equation of state.

The simplest variant of such approach is proposed in our article to describe hot white dwarfs, whose nuclear subsystem can be considered as a classical gas. We have also approximately taken into account the incomplete degeneracy of the electron subsystem. The electron subsystem in our work is treated almost in the same way as in the Fowler-Chandrasekhar model, but the nuclear subsystem is treated as in the theory of main sequence normal stars. Since the nuclear subsystem contributes to the total internal pressure, the mass and radius of the white dwarf in this model are greater than in the standard Chandrasekhar model that corresponds to the observed data. The mass-radius curves calculated by us

Table 3. The characteristics and the model parameters for the group of white dwarfs of spectral class DA from the catalog Tremblay et al. (2011) at $B \neq 0$ ($\tilde{C} = 0.142$).

Number	R/R_0	M/M_0	x_0	μ_e	ρ_c, 10^6 g cm^{-3}	T_c, 10^9 K
2922	2.82645	0.135105	0.469604	1.99206	0.201694	0.202473
1246	2.64303	0.142034	0.505594	2.00879	0.251712	0.217990
2606	2.49710	0.152426	0.544676	2.00578	0.314711	0.234840
2090	2.15203	0.183604	0.664536	2.00011	0.571548	0.286519
2507	1.98346	0.200926	0.739257	2.00529	0.786835	0.318735

agree with the distribution of observed white dwarfs on the mass-radius plane. Herewith, the calculated radii of white dwarfs can exceed the corresponding values in Chandrasekhar's theory by 2-3 times.

The Fowler-Chandrasekhar model has dimensionless parameters x_0 and μ_e. The parameter $\tilde{C}$ reflects the partial pressure of the nuclear subsystem. We determine this parameter for a specific white dwarf based on the condition that the theoretically calculated mass-radius curve for a given $\tilde{C}$ passes through the point corresponding to the observed mass and radius of the white dwarf. After that the parameters x_0 and μ_e are determined from relations (43). This allows us to calculate all characteristics for a specific white dwarf (the distribution of matter and the temperature along the radius, moment of inertia, total energy and etc.).

References

Adams, W. S., The Spectrum of the Companion of Sirius. 1915, *Publications of the Astronomical Society of the Pacific*, **27**, 236, DOI: 10.1086/122440

Bisnovatyi-Kogan, G. S., The Critical Mass of a Hot Isothermal White Dwarf with General Relativistic Effects Taken into Account. 1966, *Soviet Astronomy*, **10**, 69

Chandrasekhar, S., The Maximum Mass of Ideal White Dwarfs. 1931, *Astrophysical Journal*, **74**, 81, DOI: 10.1086/143324

Eddington, A. S. 1926, *The Internal Constitution of the Stars* (Cambridge University Press)

Fowler, R. H., On dense matter. 1926, *Monthly Notices of the Royal Astronomical Society*, **87**, 114, DOI: 10.1093/mnras/87.2.114

James, R. A., The Structure and Stability of Rotating Gas Masses. 1964, *The Astrophysical Journal*, **140**, 552, DOI: 10.1086/147949

Kaplan, S. A., Energy sources and evolution of white dwarfs. 1949, *Scientific notes of Lviv University*, **15**, 101

Kaplan, S. A., Cooling of white dwarfs. 1950, *Astron. Zhurn.*, **27**, 31

Marshak, R. E., The Internal Temperature of White Dwarf Stars. 1940, *Astrophysical Journal*, **92**, 321, DOI: 10.1086/144225

Schatzman, E., Analyse du diagramme de Hertzsprung-Russell dans la région des naines blanches (complément à la théorie du débit d'énergie des naines blanches). 1947, *Annales d'Astrophysique*, **10**, 19

Shapiro, S. L. & Teukolsky, S. A. 1983, *Black Holes, White Dwarfs and Neutron Stars* (Cornell University)

Tremblay, P. E., Bergeron, P., & Gianninas, A., An Improved Spectroscopic Analysis of DA White Dwarfs from the Sloan Digital Sky Survey Data

Release 4. 2011, *The Astrophysical Journal*, **730**, 128, DOI: 10.1088/0004-637X/730/2/128

Vavrukh, M. V., Dzikovskyi, D. V., & Smerechynskyi, S. V., Consideration of the Competing Factors in Calculations of the Characteristics of Non-Magnetic Degenerate Dwarfs. 2018, *Ukrainian Journal of Physics*, **63**, 777, DOI: 10.15407/ujpe63.9.777

Vavrukh, M. V. & Smerechynskyi, S. V., A finite temperature chandrasekhar model: Determining the parameters and calculation of the characteristics of degenerate dwarfs. 2012, *Astronomy Reports*, **56**, 363, DOI: 10.1134/S1063772912050071

Vavrukh, M. V. & Smerechynskyi, S. V., Hot degenerate dwarfs in a two-phase model. 2013, *Astronomy Reports*, **57**, 913, DOI: 10.1134/S1063772913100065

Synthetic light curves and orbital solutions of two eclipsing binary systems, V675 Lac and USNO-A2.0 1425-02035807

M.S. Alenazi[1] and M.M. Elkhateeb[2]

[1] *Physics Dept., Faculty of Science, Northern Border University, Arar, 91431-1321, Saudi Arabia*

[2] *Astronomy Dept., National Research Institute of Astronomy and Geophysics (NRIAG), 11421, Helwan, Cairo, Egypt*

Abstract. We carried out light curve modeling for all-light curves of the variable W UMa systems V675 Lac and USNO-2035807 using ground-based observations, the Gaia 3rd data release, and ZTF databases by means of the W-D code. The accepted models revealed absolute and physical parameters, which showed that the primary components in both systems are massive and hotter than the secondary ones, and both systems were classified as overcontact. A period study of the system V675 Lac of 19 year duration shows a smooth period increase with the rate $dP/dE = 1.8936 \times 10^{-10}$ day/cycle. Investigation of the systems evolutionary status showed that the primary components for both systems are situated on the ZAMS track, while their secondary components are situated above the TAMS track.

Key words: detached, binaries: contact – stars: modelling – stars: evolutionary

1. Introduction

Eclipsing binaries are always considered as a crucial astrophysical tool for researching star formation and stellar structure, testing evolutionary hypotheses, and figuring out and determining the physical characteristics of stars. They have served as benchmark candles for measuring the galaxy's size and structure as well as for setting limits on the cosmological distance scale (Bonanos et al., 2006). Calculations of absolute parameters of eclipsing binary components (radii, temperatures, mass, luminosity, etc.) from combined photometry and spectroscopy are useful for distance determination (Vilardell et al., 2010). Studies of eclipsing binaries frequently combine data from photometric sources (light curves) and spectroscopic ones (radial velocity curves). The orbital solution and light curve modeling reveal some stellar parameters, in principle, the mean surface effective temperatures of the system components, relative stellar sizes and shapes, orbital inclinations, mass ratios, and the ratios of surface

brightness. These estimated parameters can be used in studying the stellar evolution of the systems. Contact binaries, also known as the W UMa stars, are low-mass eclipsing binary systems with ellipsoidal components of orbital periods less than 1 d and continuously changing brightness (Kang et al., 2002; Percy, 2007). Most components of the W UMa type binaries share a common envelope with the same entropy, thereby making their effective temperatures almost equal over the surfaces (Paczyński et al., 2006). The structure of this paper is as follows: Section 2 deals with the basic information of the studied systems and the derivation of their times of minima. Section 3 is devoted to the light curve modeling. Section 4 presents the evolutionary status of the studied systems. Finally, Section 5 outlines our discussion and conclusions.

2. Observations and times of minima

The system USNO-A2.0 1425-02035807 ($P = 0.^d31618$) (hereafter refer as to as USNO-2035807) was announced as a new discovered variable of W UMa type eclipsing binaries by Liakos (2019). It was detected in the field of view of the planetary nebula Sh2-188 and classified as a W UMa system in the GCVS and AAVSO databases. First observations of the system in the red (Bessell) photometric filter were carried out by Liakos (2019) at the Kryoneri Observatory of the National Observatory of Athens, Corinthia, Greece, between November 2017 and September 2019 using a 1.2-m prime focus telescope (f/3) equipped with the APOGEE ASPEN CG47 CCD camera. The stars USNO-A2.01425-02037041 and USNO-A2.01425-02034268 were used as comparison and check stars, respectively. The system GSC 03208-01986 (hereafter referred to as V675 Lac) was initially included in the Tycho catalog (TYC 3208-1986-1) with V = 11.20 and (B-V) = 0.48 (Hog et al., 1998). It was observed (unfiltered) as an NSVS variable from May 1, 1999, to February 1, 2000. The observed light curve was phased with a period of 0.404567 days and demonstrated that the system V675 Lac belongs to the W UMa binary. The system was included in the bright contact binary stars cataloged by Gettel et al. (2006) from ROTSE observations. Liakos & Niarchos (2011) observed the system on July 21–24 and August 1–3, 2010, using a 0.2 m reflector f/5 telescope at the University of Athens Observatory, Greece, in BI filters. Samec et al. (2015) (hereafter 2015-Samec) observed the system V675 Lac during four nights from 24 to 29 September, 2012, which revealed complete UBVRcIc light curves. The extensive observations from SWASP give us the opportunity to solve well-defined light curves for the years 2004, 2006, and 2007. The data for 2007 is the best and most numerous. A new BVRcIc light curve was observed by Polakis in 2017 and 2018 (hereafter 2017-Polakis and 2018-Polakis) (Eaton et al., 2019). In addition to ground-based observations, we tried to collect all available photometric observations for the studied systems from miscellaneous astronomical databases to increase the accuracy of the adopted models. A set of photometric observations were obtained

**Table 1.** Basic information on the variable, comparison, and check stars.

Star Name	R.A. (2000)	Dec. (2000)	B	V	B-V
V675 Lac	$22^\mathrm{h}\ 25'16.03''$	$+41°27'52.00''$	12.01	11.52	0.49
GSC 03208-02737 (comparison)	$22^\mathrm{h}\ 24'26.84''$	$+41°23'42.86''$	11.63	11.27	0.36
GSC 03208-02740 (check)	$22^\mathrm{h}\ 14'10.32''$	$+41°23'36.64''$	11.21	10.22	0.99
USNO-2035807	$01^\mathrm{h}\ 30'15.40''$	$+58°27'32.20''$	–	16.99	–
USNO-A2.0 1425-02037041 (comparison)	$01^\mathrm{h}\ 30'18.81''$	$+58°23'10.96''$	–	18.10	–
USNO-A2.0 1425-02034268 (check)	$01^\mathrm{h}\ 30'10.95''$	$+58°27'33.16''$	19.20	–	–

from the Gaia 3rd data release (Gaia Collaboration et al., 2016, 2023) for the systems V675 Lac and USNO-2035807 in BVR and VR passbands, respectively. Complete light curves for the system USNO-2035807 in VRI passbands were obtained from the ZTF database. Ephemeris formulas in Equation (1) adopted by Odell (Eaton et al., 2019) (derived from the NSVS plus 2017-Polakis data) and Equation (2) by Liakos (2019), are used to estimate the relevant phases of each observation for the system V675 Lac and USNO-2035807, respectively. Figure 1(a),(b) displays the observed light curves for the system V675 Lac by Liakos & Niarchos (2011) data and by the Gaia 3rd data release respectively. Figure 2 (a)–(d) displays the observed light curves by SWASP 2007, Samec et al. (2015), 2017-Polakis, and 2018-Polakis, respectively . The observed light curves of the system USNO-2035807 are displayed in Figure 3(a)-(c) for ground-based observations by Liakos (2019), Gaia 3rd data release, and ZTF data, respectively.

$$MinI = HJD2456194.7011 + 0.4045663 \times E. \tag{1}$$
$$MinI = HJD2458081.4380 + 0.3161800 \times E. \tag{2}$$

The orbital period of the system V675 Lac was studied by 2015-Samec using times of minima revealed from their observations together with estimated minima from the NSVS and Liakos & Niarchos (2011) light curves. A smooth period decrease was derived, corresponding to a timescale of 13 years (12000 orbits). Eaton et al. (2019) point out that period decrease results from 2015-Samec are not acceptable for what they claim is an "ancient" contact system, especially
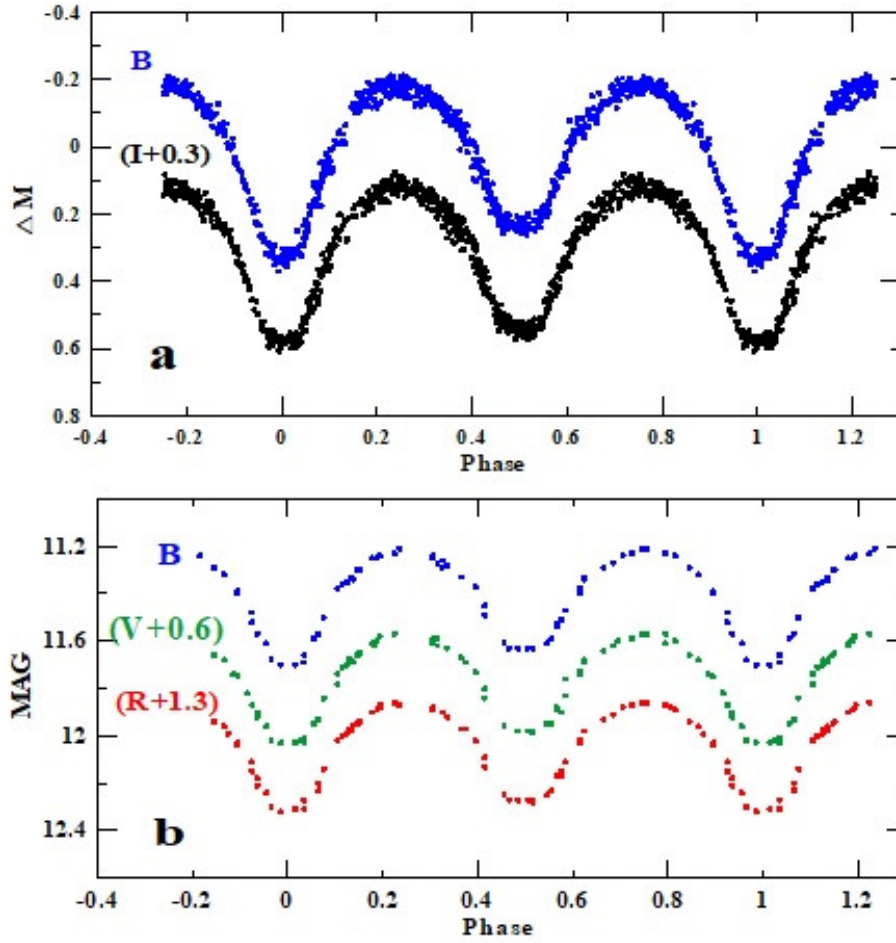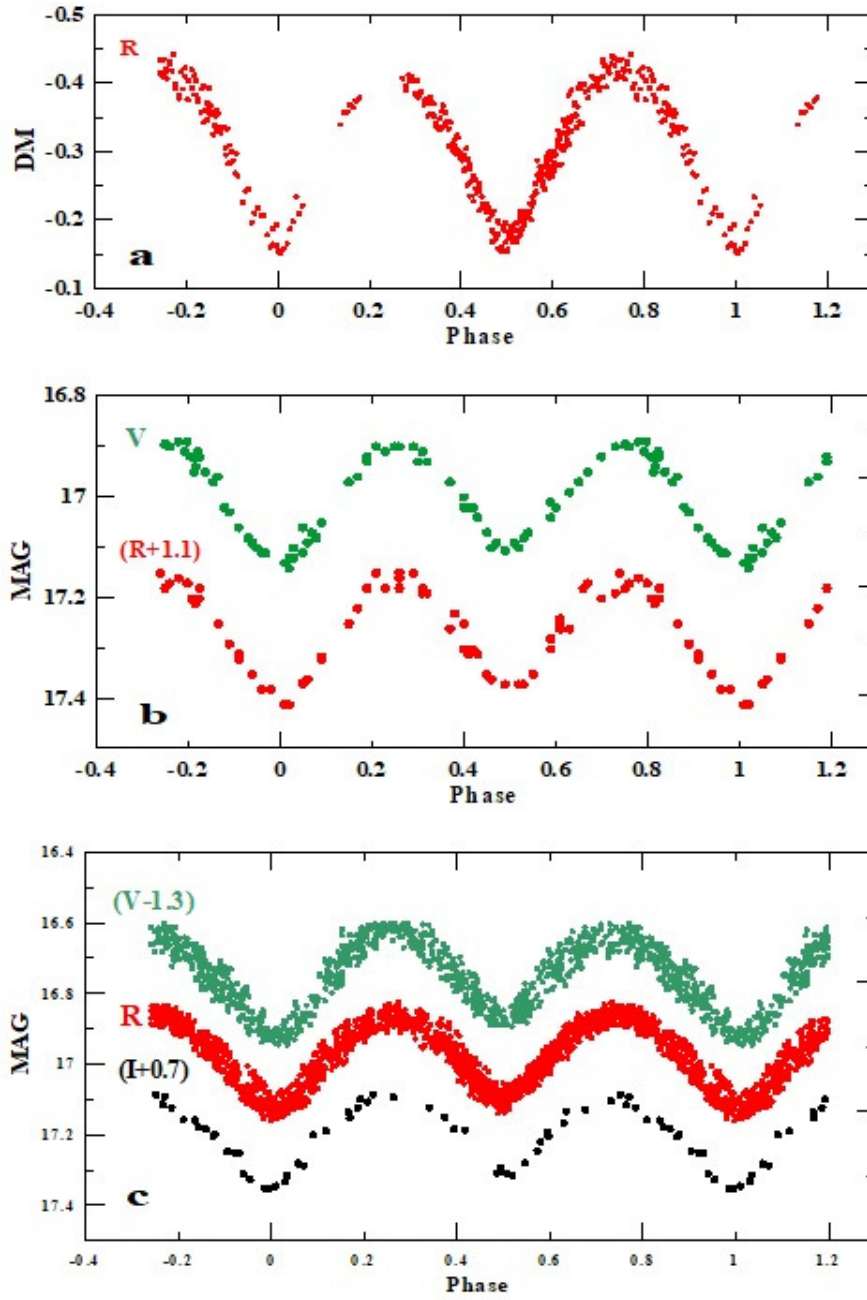
Figure 1. Observed light curves for the system V675 Lac: (a) Liakos & Niarchos (2011) data and (b) the Gaia 3rd data release.

if caused by magnetic braking, their forward period-change mechanism. They refer to the radical period decrease as resulting from the Samec's previously documented error of confusing the Modified Jullian Date (Heliocentric Jullian Date HJD - 2400000.5) with the Reduced Jullian Date (HJD - 2400000.0) in data from the Northern Sky Variability Survey (Woźniak et al., 2004). Eaton et al. (2019) downloaded archival data from NSVS and SuperWasp (SWASP) websites, also obtained new light curves by Polakis for 2017 and 2018 (BVRcIc on the UBV/Cousins system) and added the published photometry of Liakos & Niarchos (2011). They collected all light curves and derived nine epochs of min-
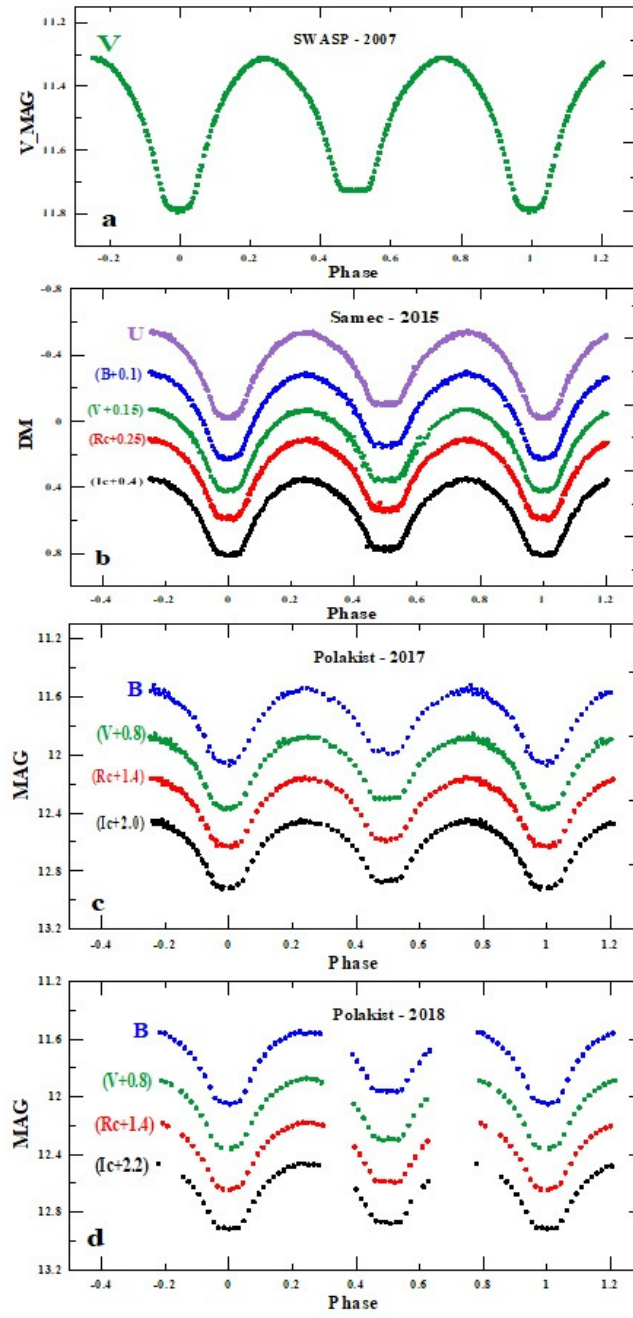
Figure 2. Observed light curves for the system V675 Lac: (a) SWASP 2007, (b) Samec et al. (2015), (c) 2017-Polakis, (d) 2018-Polakis.

Figure 3. Observed light curves for the system USNO-2035807: (a) Liakos (2019), (b) The Gaia 3rd data release and (c) The ZTF data.

**Table 2.** Light minima for the systems V675 Lac and USNO-2035807.

HJD	Error	Min	Epochs (E)	(O-C)	(O-C)q	Ref.
			V675 Lac			
2451464.1096	0.0010	I	-11693	0.0022	-0.0005	1
2453247.4351	0.0003	I	-7285	-0.0005	0.0007	2
2453989.8134	0.0006	I	-5450	-0.0014	0.0005	3
2454324.7939	0.0001	I	-4622	-0.0018	0.0001	4
2454374.1509	0.0001	I	-4500	-0.0019	0.0000	5
2455400.5369	0.0006	I	-1963	-0.0006	0.0006	6
2455402.5593	0.0003	I	-1958	-0.0010	0.0002	6
2455410.4491	0.0003	II	-1938.5	-0.0012	0.0009	6
2455411.4591	0.0003	I	-1936	-0.0017	-0.0005	6
2456194.7010	0.0001	I	0	-0.0001	-0.0003	7
2456196.7237	0.0002	I	5	-0.0002	-0.0004	7
2456196.9266	0.0011	II	5.5	0.0004	0.0002	7
2456197.7353	0.0002	II	7.5	-0.0001	-0.0003	7
2456197.7356	0.0002	II	7.5	0.0003	0.0001	7
2456197.9368	0.0002	I	8	-0.0008	-0.0010	7
2456199.7584	0.0004	II	12.5	0.0002	0.0000	7
2456199.7586	0.0005	II	12.5	0.0004	0.0002	7
2457924.8343	0.0003	II	4276.5	0.0054	-0.0003	8
2457924.8346	0.0006	II	4276.5	0.0057	0.0000	8
2457924.8349	0.0002	II	4276.5	0.0060	0.0003	8
2457927.8684	0.0002	I	4284	0.0053	-0.0005	8
2458415.7778	0.0002	I	5490	0.0077	-0.0002	9
2458415.7779	0.0004	I	5490	0.0078	-0.0001	9
2458416.7898	0.0002	II	5492.5	0.0083	0.0004	9
2458416.7902	0.0001	II	5492.5	0.0087	-0.0005	9
			USNO-2035807			
2458368.5300	0.0004	I	908	0.0006	—	10
2458340.5482	0.0005	II	819.5	0.0007	—	10
2458346.5559	0.0004	II	838.5	0.0010	—	10
2458364.5761	0.0004	II	895.5	-0.0011	—	10

References: 1-NSVS, 2-SWASP (2004) , 3-SWASP (2006), 4-SWASP (2007), 5-SWASP (2007) Epoch2, 6-Liakos & Niarchos (2011), 7-Samec et al. (2015), 8-2017-Polakis, 9-2018-Polakis, 10-Liakos (2019).

ima, which fitted and showed that the system's period is increasing moderately on a timescale of 2×10^6 years, which is a very different result than 2015-Samec.

In the present paper, we used the package Minima V2.3 (http://members. shaw.ca/bob.nelson/software1.html) to estimate times of minima from the seven observed light curves displayed in Figure 1(a), (b) for data from Liakos & Niarchos (2011) and the Gaia 3rd data release, and in Figure 2(a)-(d) for the data from SWASP 2007, 2015-Samec, 2017-Polakis and (2018) together with
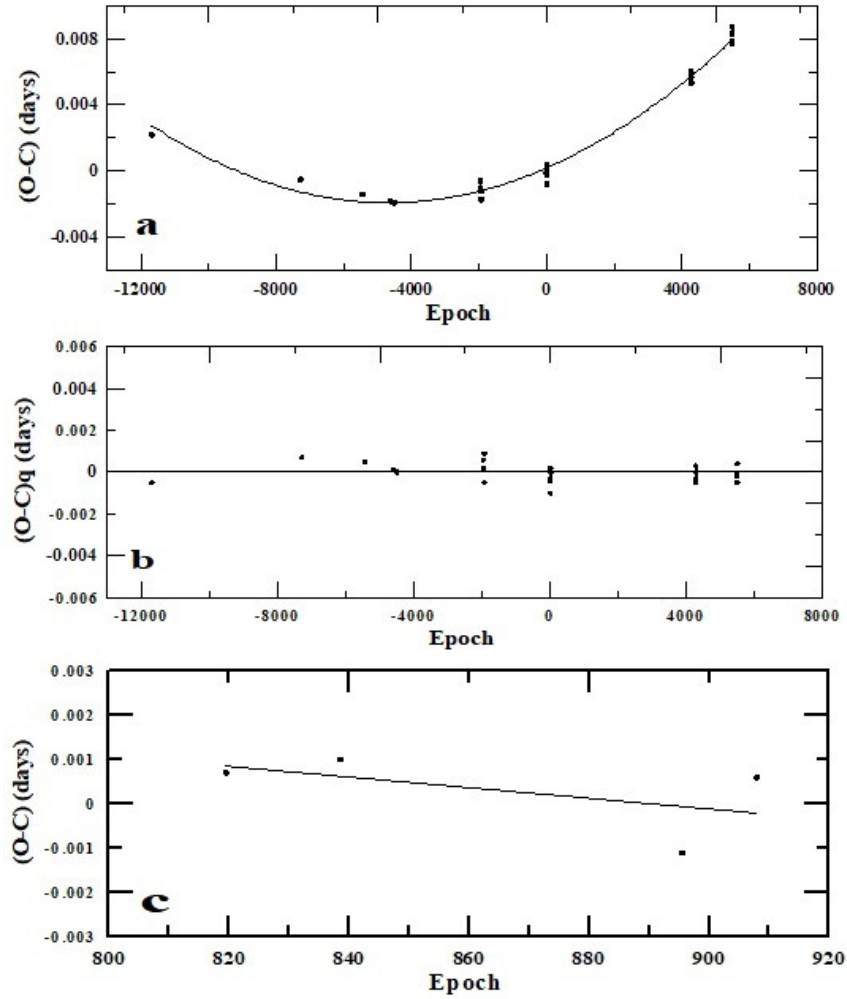
Figure 4. Period behavior of the systems: (a,b) V675 Lac, and (c) USNO-2035807.

light curves downloaded from NSVS. A total of 25 minima were estimated from the observed light curves. The orbital period of the system V675 Lac was studied by means of an O-C diagram using 25 epochs of minima derived from all available light curves spanning the time interval from 1999 to 2018, covering about 19 years (17142 revolutions). In the residuals (O-C), the C's were calculated using the linear elements in Eq. (1) and are listed in Table 2. Figure 4a represents the O-C values versus the Epoch (E) for the system V675 Lac; no distinctions have been made between primary and secondary minima. The general trend of

the O-C diagram can be represented by a quadratic fit with a residual sum of squares of 4.318×10^{-6} and an R-squared of 0.987, yielding the following:

$$MinI = 2456194.7013 + 0.^{d}404567188 \times E + 0.9468 \times 10^{-10} \times E^2. \qquad (3)$$

Light elements of Eq. (3) give a new period (P $= 0.^{d}404567188$); the period shows an increase with the rate $dP/dE = 1.8936 \times 10^{-10} day/cycle$ or $1.7084 \times 10^{-7} day/year$ or 2 second/century. The O-C residuals calculated using the quadratic ephemeris of Eq. (3) are listed in Table 2 and displayed in Figure 4b. A total of four minima were estimated for the system USNO-2035807 from the observed light curves and listed in Table 2. The residuals (O-C) and C's, were calculated using the linear elements in Eq. (2) and are listed in Table 2. As the system USNO-2035807 was discovered a few years ago and has no data base of observations (times of minima), we used the available times of minima listed in Table 2 to construct a preliminary view of the period behavior of the system using the estimated O-C values represented by a linear fit, as illustrated in Figure 4c.

3. Light curve modeling

The observed light curves of the systems V675 Lac and USNO-2035807 indicate typical short-period W UMa eclipsing binaries with continuous changes in brightness with nearly equal depth minima and maxima. Photometric analyses of the systems were carried out using the synthetic light curve and differential corrections program of the Wilson and Devinney code (W-D) (Wilson et al., 2020), which was based on the Milone (1993) model atmosphere. Mode 3 of the code was applied to the observed light curves during the calculations for both systems. We used the B-V values published for the systems at SIMBAD (http://simbad.u-strasbg.fr/simbad/) to calculate the corresponding initial temperature for the primary components T_1 using the Cox (2000) relation. The observed light curves were analyzed using all individual observations in each band. Gravity darkening (A_1, A_2) and bolometric albedo (g_1, g_2) exponents were assumed for the convective envelopes (Teff<7500 K) of the late spectral type, and we adopted $A_1 = A_2 = 0.5$ (Ruciński, 1969) and $g_1 = g_2 = 0.32$ (Lucy, 1967).

The bolometric limb darkening coefficients were adopted and interpolated using the logarithmic law for the extinction coefficients from van Hamme (1993). To establish the initial mass ratio (q), a q-search method was used because spectroscopic measurements (radial velocity) for the systems under study are not available. Therefore, some test solutions for a range of assumed mass ratios (q) with values spanning from 0.10 to 0.90 were performed. Figure 5(a),(b) shows the plotting of the sum of the squared deviations $\sum(O - C)^2$ for every q value for all studied systems. The starting points for modeling are the values of q, which correspond to the minima of $\sum(O - C)^2$ found for each system.
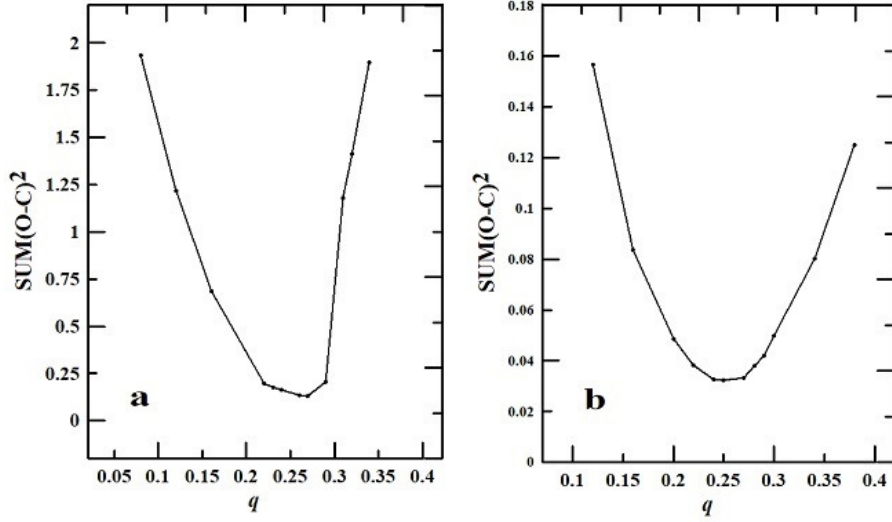
Figure 5. q-search of the binary systems: a) V675 Lac, b) USNO-2035807.

Table 3. Orbital solution parameters for the system USNO-2035807.

Parameter	(Liakos data)	ZTF data	(Gaia data)
$i[°]$	57.81±0.16	58.31±0.25	57.00±0.20
$g_1 = g_2$	0.32	0.32	0.32
$A_1 = A_2$	0.5	0.5	0.5
$q(M_2/M_1)$	0.2590±0.0012	0.2486±0.0021	0.2605±0.0023
$\Omega_1=\Omega_2$	2.2677±0.0026	2.2640±0.0045	2.3119±0.0056
T_1 [°K]	4489±5	4355±11	4496±43
T_2 [°K]	4207±4	4240±6	4196±8
Ω_{in}	2.3736	2.3496	2.3772
Ω_{out}	2.2107	2.1928	2.2134
r_1 pole	0.4914±0.0030	0.4900±0.0050	0.4814±0.0044
r_1 side	0.5385±0.0046	0.5361±0.0075	0.5241±0.0065
r_1 back	0.5718±0.0064	0.5670±0.0103	0.5534±0.0089
r_2 pole	0.2774±0.0062	0.2694±0.0108	0.2669±0.0099
r_2 side	0.2931±0.0080	0.2838±0.0137	0.2802±0.0124
r_2 back	0.3592±0.0237	0.3410±0.0358	0.3286±0.0282
$\sum$ (O-C)^2	0.44563	0.02230	0.00714

Table 4. Orbital solution parameters for the system V675 Lac.

Parameter	Liakos& Niarchos 2011	Gaia data	Samec et al. (2015)	SWASP 2007	2017-Polakis	2018-Polakis
$i[°]$	85.79±0.51	86.31±2.14	85.09 (fixed)	85.09 (fixed)	85.09 (fixed)	85.09 (fixed)
$g_1 = g_2$	0.32	0.32	0.32	0.32	0.32)	0.32)
$A_1 = A_2$	0.5	0.5	0.5	0.5	0.5	0.5
$q(M_2/M_1)$	0.2791±0.0009	0.2713±0.0017	0.2636±0.0005	0.2657±0.0011	0.2675±0.0010	0.2664±0.0009
$\Omega_1=\Omega_2$	2.3855±0.0028	2.3685±0.0039	2.3518±0.0012	2.3485±0.0032	2.3499±0.0032	2.3585±0.0028
T_1 [°K]	6675±15	6718±13	6736±3	6579±22	6639±26	6663±6
T_2 [°K]	6449±7	6471±9	6455±3	6406±9	6453±8	6468±14
Ω_{in}	2.4195	2.4019	2.3843	2.3891	2.3931	2.3906
Ω_{out}	2.2447	2.2317	2.2187	2.2222	2.2252	2.2233
r_1 pole	0.4689±0.0013	0.4710±0.0021	0.4732±0.0005	0.4743±0.0014	0.4743±0.0007	0.4723±0.0013
r_1 side	0.5071±0.0019	0.5098±0.0029	0.5125±0.0007	0.5142±0.0020	0.5143±0.0010	0.5113±0.0019
r_1 back	0.5342±0.0024	0.5367±0.0038	0.5392±0.0009	0.5416±.0025	0.5419±0.0012	0.5381±0.0024
r_2 pole	0.2638±0.0022	0.2617±0.0037	0.2596±0.0008	0.2621±0.0022	0.2631±0.0008	0.2602±0.0021
r_2 side	0.2757±0.0027	0.2735±0.0046	0.2713±0.0010	0.2742±0.0027	0.2753±0.0009	0.2719±0.0025
r_2 back	0.3149±0.0053	0.3128±0.0089	0.3105±0.0019	0.3153±0.0053	0.3170±0.0017	0.3110±0.0049
$\sum$ (O-C)^2	0.1344	0.0103	0.0646	0.0057	0.0217	0.0036

The adjustable parameters were: the mass ratio (q), the inclination (i), the temperature of the primary star (T_1) and the secondary one (T_2), the surface potential ($\Omega_1 = \Omega_2$, for over-contact systems), and the monochromatic luminosity of the primary star (L_1). The relative brightness of the secondary star (L_2) was calculated by the stellar atmosphere model. The photometric analysis was performed on all the observed light curves of the studied systems, and some trials were conducted to find a set of parameters that roughly correspond to the observed light curves. After applying the WD code (Wilson et al., 2020) condition of Mode 3 (over-contact), the best photometric fitting was obtained, and synthetic light curves were estimated for each system. The first light curve modeling for the system V675 Lac was carried out by 2015-Samec using his UB-VRcIc light curves. Mode 3 (over contact) of the W-D code was applied with the starting values of the parameters estimated from BM3 (Bradstreet & Steelman, 2002). No third body was included in their constructed model, and a set of parameters were estimated that classified the system as totally eclipsing classic A-Type W UMa binary. Eaton et al. (2019) present a light curve analysis for the system V675 Lac using SWASP observed light curves in the years 2004 and 2007 (the quality of 2007 data are the better than that of 2004 (Eaton et al., 2019)) together with observed light curves by Polakis in 2017 and 2018. The W-D code was used to solve the collected light curves, and a set of absolute parameters was estimated according to the constructed model. Their accepted model for SWASP 2004 and SWASP 2007 light curves reveals a small dark spot on the leading hemisphere of the primary component, which does not appear in the model of Pokalis (2017) and (2018) light curves.

**Table 5.** Physical parameters for the system USNO-2035807.

Parameter	(Liakos data)	ZTF data	(Gaia data)
$M_1(M_\odot)$	0.6627±0.0271	0.6153±0.0251	0.6651±0.0272
$M_2(M_\odot)$	0.1716±0.0070	0.1530±0.0063	0.1733±0.0071
$R_1(R_\odot)$	0.7493±0.0306	0.6985±0.0285	0.7519±0.0307
$R_2(R_\odot)$	0.6423±0.0262	0.6549±0.0267	0.6382±0.0261
$L_1(L_\odot)$	0.2043±0.0083	0.1572±0.0064	0.2070±0.0085
$L_2(L_\odot)$	0.1158±0.0047	0.1242±0.0051	0.1131±0.0046
$T_1(T_\odot)$	0.7769±0.0317	0.7537±0.0308	0.7781±0.0318
$T_2(T_\odot)$	0.7281±0.0297	0.7338±0.0300	0.7262±0.0298
M_{bol1}	6.4745±0.2643	6.7586±0.2759	6.4602±0.2637
M_{bol2}	7.0909±0.2895	7.0148±0.2864	7.1161±0.2905
M_{v1}	7.2287±0.2951	7.6238±0.3112	7.2090±0.2943
M_{v2}	8.0952±0.3305	7.9865±0.3261	8.1315±0.3320
Sp. Type	$(K4)^1, (K7)^2$	$(K5)^1, (K6)^2$	$(K4)^1, (K7)^2$

Note: 1 and 2 refer to the primary and secondary components, respectively.

**Table 6.** Physical parameters for the system V675 Lac.

Parameter	Liakos& Niarchos (2011)	Gaia data	Samec et al. (2015)	SWASP 2007	2017-Polakis	2018-Polakis
$M_1(M_\odot)$	1.4034±0.0573	1.4170±0.0579	1.4227±0.0581	1.3728±0.0560	1.3919±0.0568	1.3995±0.0571
$M_2(M_\odot)$	0.3917±0.0160	0.3844±0.0157	0.3750±0.0153	0.3648±0.0149	0.3723±0.0152	0.3728±0.0152
$R_1(R_\odot)$	1.4779±0.0603	1.4898±0.0608	1.4948±0.0610	1.4509±0.0592	1.4678±0.0599	1.4746±0.0602
$R_2(R_\odot)$	1.4137±0.0577	1.4201±0.0580	1.4154±0.0578	1.4012±0.0592	1.4149±0.0578	1.4192±0.0579
$L_1(L_\odot)$	3.8849±0.1586	4.0505±0.1654	4.1216±0.1683	3.5335±0.1443	3.7500±0.1531	3.8399±0.1568
$L_2(L_\odot)$	3.0972±0.1264	3.1682±0.1293	3.1163±0.1272	2.9624±0.1209	3.1102±0.1270	3.1583±0.1289
$T_1(T_\odot)$	1.1552±0.0472	1.1627±0.0475	1.1658±0.0476	1.1386±0.0465	1.1386±0.0465	1.1532±0.0471
$T_2(T_\odot)$	1.1161±0.0456	1.1199±0.0457	1.1172±0.0456	1.1087±0.0453	1.1168±0.0456	1.1194±0.0457
M_{bol1}	3.2765±0.1338	3.2312±0.1319	3.2123±0.1311	3.3795±0.1380	3.3149±0.1353	3.2892±0.1343
M_{bol2}	3.5226±0.1438	3.4980±0.1428	3.5159±0.1435	3.5709±0.1458	3.5180±0.1436	3.3740±0.1377
M_{v1}	3.3610±0.1372	3.3148±0.1353	3.2956±0.1345	3.4670±0.1415	3.4003±0.1388	3.5014±0.1429
M_{v2}	3.6165±0.14	3.5906±0.1466	3.6095±0.1474	3.6676±0.1497	3.6117±0.1475	3.5942±0.1467
Sp. Type	$(F5)^1,(F6)^2$	$(F4)^1,(F6)^2$	$(F4)^1,(F6)^2$	$(F6)^1,(F7)^2$	$(F5)^1,(F6)^2$	$(F5)^1,(F6)^2$

Note: 1 and 2 refer to the primary and secondary components, respectively.
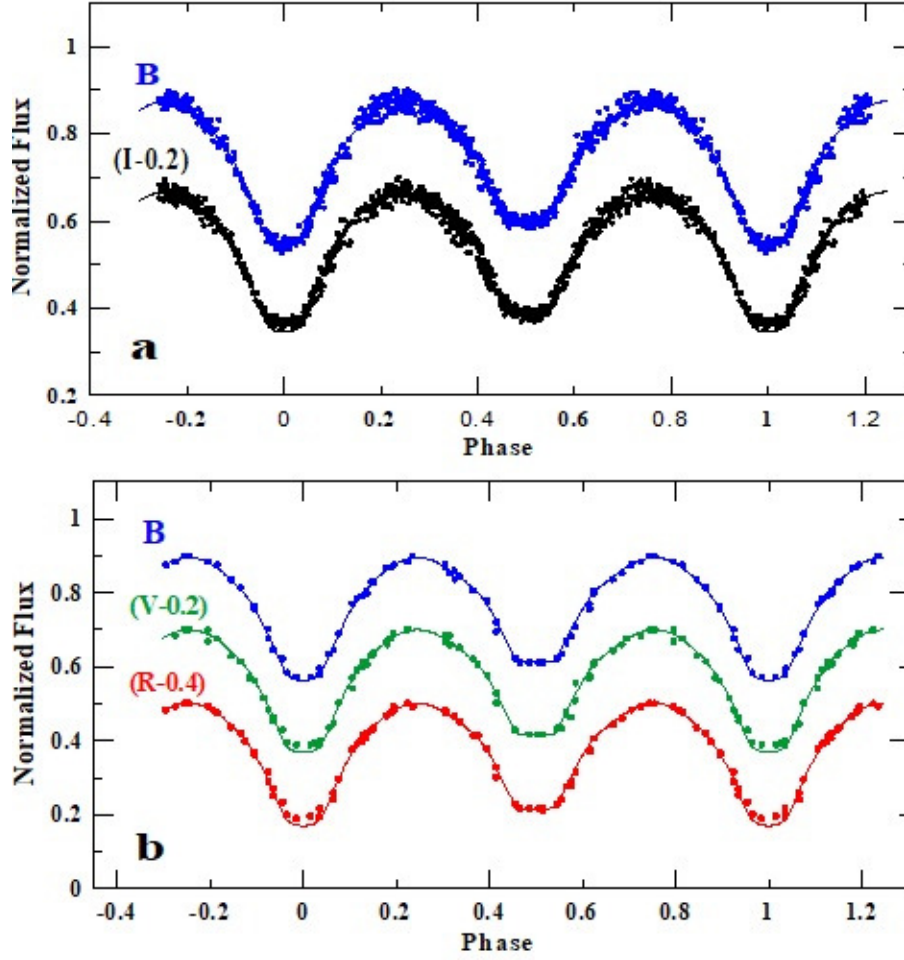
Figure 6. The light curve solutions for the systems V675 Lac: (a) Liakos & Niarchos (2011) data and (b) The Gaia 3rd data release; synthetic (lines) and observed (dots).

As Samec et al. (2015) used only his own light curves, Eaton et al. (2019) used just three observed light curves to construct their orbital solution, in the present paper we collected all ground-based observations: SWASP 2007, Liakos & Niarchos (2011), Samec et al. (2015), 2017-Polakis and (2018), together with observations downloaded from the Gaia3rd data release (Gaia Collaboration et al., 2016, 2023). A total of six complete sets of light curves were used through Mode 3 of the W-D code to construct a model-represented orbital solution for all available light curves of the system V675 Lac. The adopted model shows
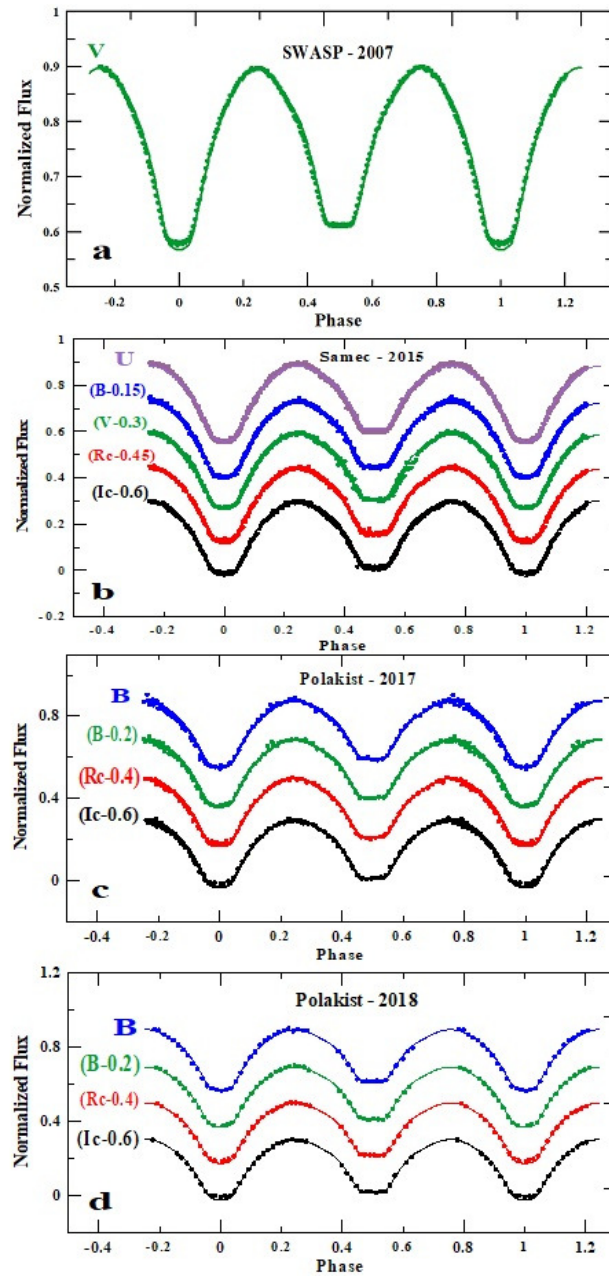
Figure 7. The light curve solutions for the systems V675 Lac: (a) SWASP 2007, (b) Samec et al. (2015), (c) 2017-Polakis, and (d) 2018-Polakis.; synthetic (lines) and observed (dots).

no spots on the primary component, as Eaton et al. (2019) suggest for SWASP 2007 observations, and demonstrates that the primary component is hotter than the secondary one. The high inclination of 85 degrees results in a long-duration secondary total eclipse. The synthetic light curve solution is given in Table 4, while the normalized curves overlain by the light curve solutions are shown in Figures 6(a), (b), and 7(a)-(d).
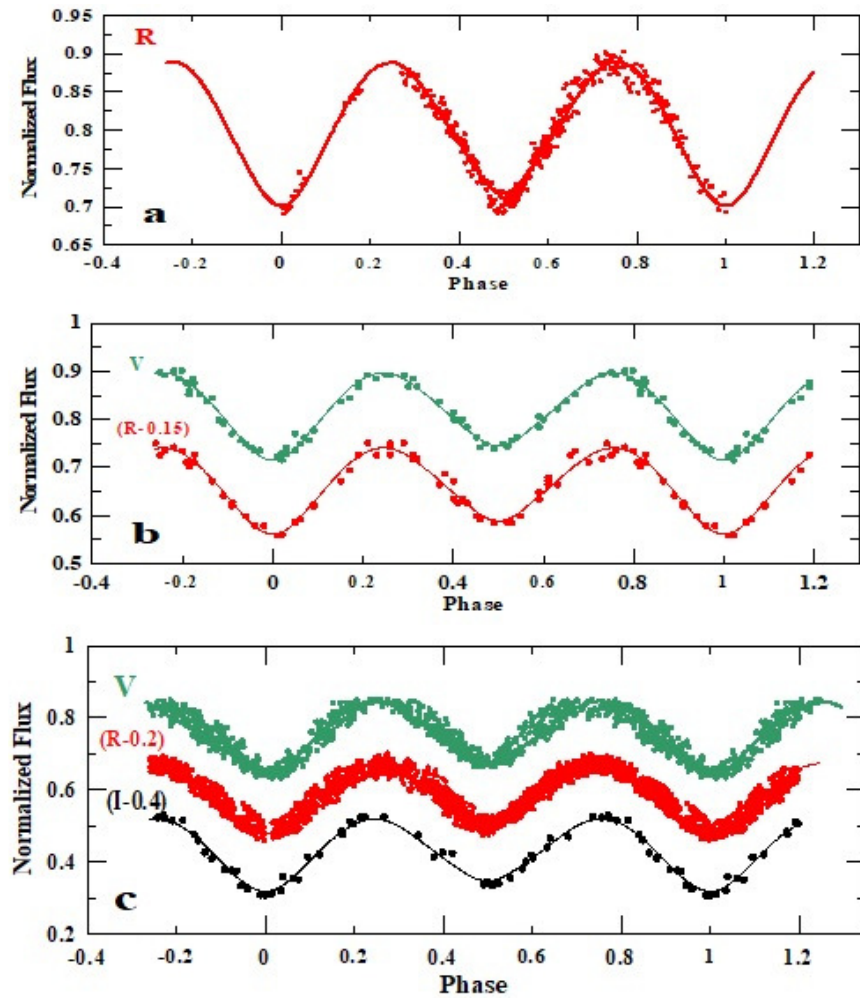
Figure 8. The light curve solutions for the system USNO-2035807: (a) Liakos (2019), (b) The Gaia 3rd data release and (c) The ZTF data; synthetic (lines) and observed (dots).

For the system USNO-2035807, we carried out the first light curve modeling using the available ground-base light curve by Liakos (2019) together with light curves downloaded from the Gaia 3rd data release and ZTF in different pass bands. The accepted solution demonstrates that the primary components are hotter than the secondary ones. Table 3 lists the estimated absolute parameters of the accepted models for each light curve, while Figures 8(a)–(c) display the synthetic and the observed light curves for the system USNO-2035807.

The calculation of the physical parameters of the eclipsing binary components is mostly estimated using spectroscopic observations of their radial velocity. Since the studied systems had no prior spectroscopic observations, the empirical Teff-mass relation provided by Harmanec (1988) was used to approximate their absolute physical parameters. Tables 5 and 6 present the absolute physical parameters that were determined for each component of the system, USNO-2035807 and V675 Lac, respectively. According to these parameters, the primary components of both systems are more massive than the secondary components. The spectral types of system components were adopted based on the parameters of the accepted orbital solutions (Popper, 1980).

The W UMa systems are subcategorized into the A-type and the W-type by Binnendijk (1970). These groups can be further divided into the A9-F8 group (A-type) and the F7-M5 group (W-type) based on their spectral types. Eaton (1983) proposed that the two types of W UMa systems can be distinguished by the presence (W-type) or absence (A-type) of magnetic spots. According to the adopted spectral types, the systems V675 Lac and USNO-2035807 can be classified as W UMa systems of the A-type and the W-type, respectively. In verifying the validity of the relation $r_1 + r_2 = 0.75$ for contact systems, according to Kopal (1959), it is found that $r_1 + r_2 = 0.8438$ for the system V675 Lac and $r_1 + r_2 = 0.7882$ for the system USNO-2035807, when using the mean values of r_1 and r_1 given in Table 3 and 4 for the studied systems. Hence, according to the calculated values, the systems V675 Lac and USNO-2035807 are overcontact eclipsing binaries with components overfilling their respective Roche lobes, as shown in Figures 9(a) and (b), which depict the three-dimensional view of the studied systems based on the calculated parameters from the adopted models using the software Package Binary Maker 3.03 of Bradstreet & Steelman (2002).

4. Evolutionary state

The mass-luminosity (M-L) and mass-radius (M-R) relations, as well as the evolutionary tracks calculated by Girardi et al. (2000) for both zero-age main sequence stars (ZAMS) and thermal-age main sequence stars (TAMS) with metallicity z = 0.019, were used to investigate the evolutionary state of the studied systems using their estimated physical parameters, which are listed in Table, 5 and 6. The primary components (S_1) for both systems are situated on the ZAMS, whilst their secondary components (S_2) are situated above the
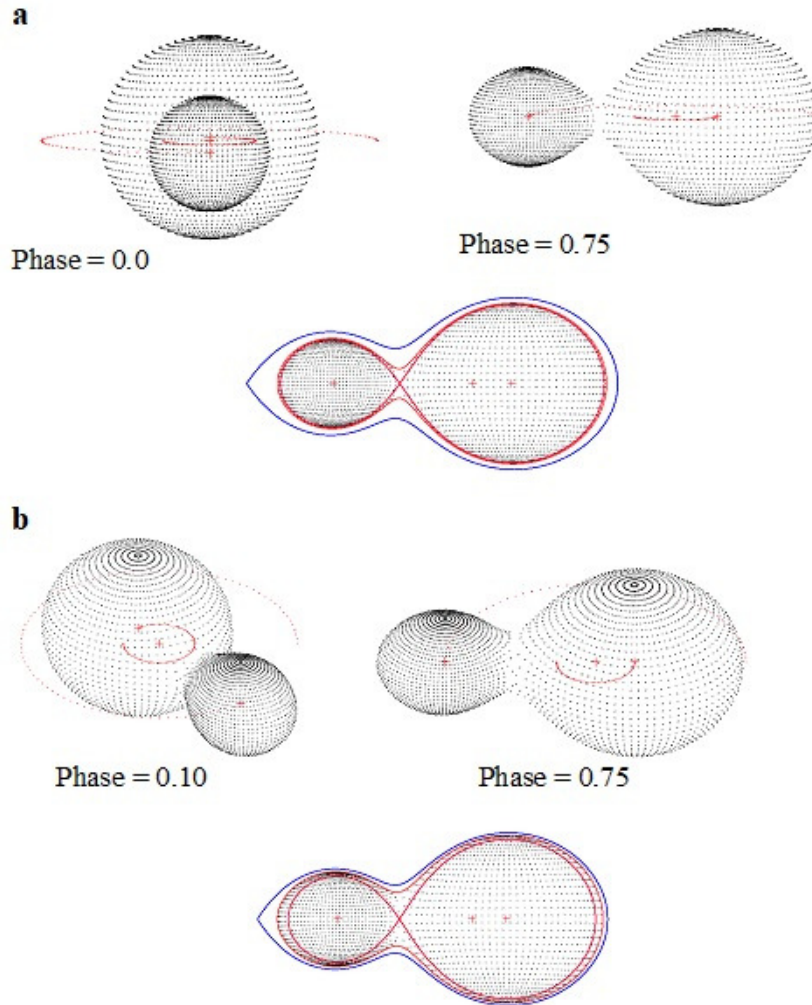
Figure 9. A three-dimensional view of the binary systems: a) V675 Lac, b) US-NO-2035807.

TAMS track as shown in Figure 10(a) and (b) which displays the locations of the studied systems components S_1 and S_2 on the M-L and M-R relations. The evolutionary states of the systems were also examined using the luminosity-effective temperature (L-Teff) relation of non-rotated models and the empirical mass-effective temperature (M-Teff) relation of the intermediate and low-mass eclipsing binaries.

All the components of the systems are located on the Teff-L, therefore, an
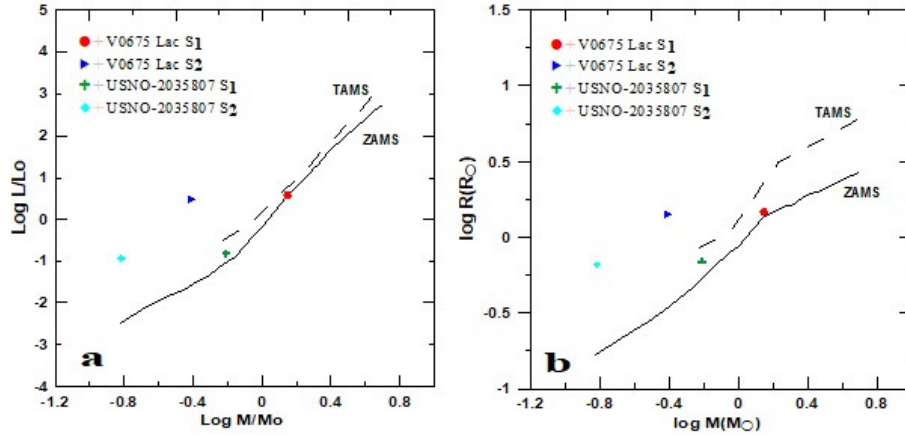
Figure 10. Positions of the components S_1, S_2 of the systems V675 Lac and US-NO-2035807 on the theoretical diagram (a) mass- luminosity, and (b) mass-radius of Girardi et al. (2000).

agreement has been achieved between the masses derived from the orbital solutions and those for the stellar models, using the non-rotated evolutionary models of Ekström et al. (2012) in the range of $0.6-2.0\ M_\odot$ at solar metallicity $z = 0.014$, as illustrated in Figure 11 where each component shows a fair fit.

Figure 12 shows the M-Teff relation for low-mass and intermediate-mass stars (Malkov, 2007), and also shows that the locations of the primary components of both systems are in good agreement while the secondary components show some deviations. Such deviations are similar to that in Figure 10(a) and (b) in the M-L and M-R diagrams; we attribute this to an energy transfer via the common convective envelope from the primary to the secondary components of both systems (Lucy (1973)).

5. Discussion and conclusions

Using all available CCD ground-based observations in various pass bands together with the Gaia 3rd data release, SWASP and the ZTF database, orbital solutions for the eclipsing binary systems V675 Lac and USNO-2035807 were carried out. The adopted models reveal a set of absolute parameters that demonstrate that all the primary components of both systems are hotter and more massive than the secondary components. A total of 29 new times of minima from the observed light curves of the studied systems were calculated, and the O-C curves were constructed. The period study of the system V675 Lac of 19-year duration shows a smooth period increase with the rate $dP/dE = 1.8936 \times 10^{-10} day/cycle$. The behavior of the studied systems in M-R and M-L relations using their evolu-
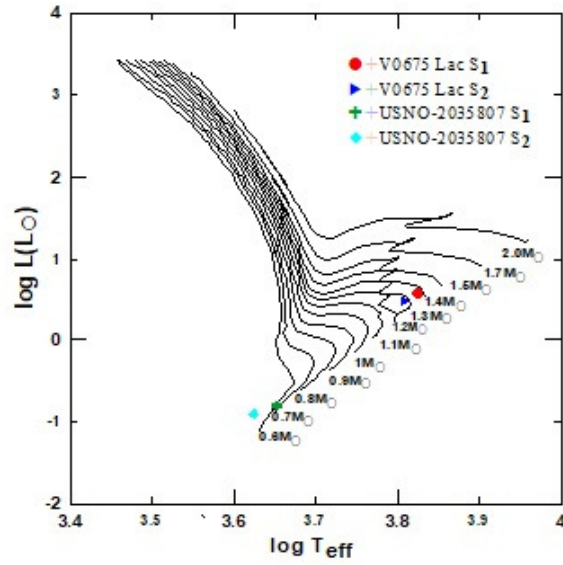
Figure 11. Positions of the components S_1, S_2 of the systems V675 Lac and US-NO-2035807 on the Teff–L diagram of Ekström et al. (2012).
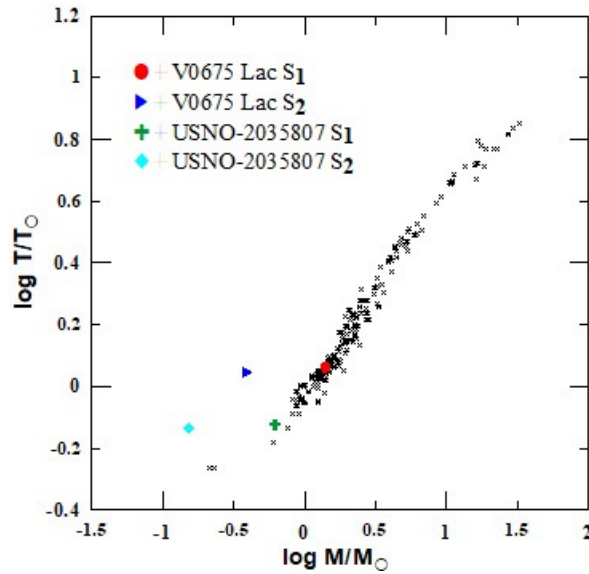
Figure 12. Positions of the components S_1, S_2 of the systems V675 Lac and US-NO-2035807 on the M-Teff diagram by Malkov (2007).

tionary states was examined. The primary components S1 for both systems are situated on the ZAMS, while their secondary components S2 are situated above the TAMS track. Such deviations are also noticed when examining the M-Teff relation for low-mass and intermediate-mass stars and can be attributed to an energy transfer from the primary to the secondary components via the shared convective envelope, which accounts for the general deviation of the secondary's in W UMa systems.

References

Binnendijk, L., The orbital elements of W Ursae Majoris systems. 1970, *Vistas in Astronomy*, **12**, 217, DOI: 10.1016/0083-6656(70)90041-3

Bonanos, A. Z., Stanek, K. Z., Kudritzki, R. P., et al., The First DIRECT Distance Determination to a Detached Eclipsing Binary in M33. 2006, *Astrophysical Journal*, **652**, 313, DOI: 10.1086/508140

Bradstreet, D. H. & Steelman, D. P., Binary Maker 3.0 - An Interactive Graphics-Based Light Curve Synthesis Program Written in Java. 2002, in American Astronomical Society Meeting Abstracts, Vol. **201**, *American Astronomical Society Meeting Abstracts*, 75.02

Cox, A. 2000, *In:Cox, N. (4th Ed.), "Allen's Astrophysical Quantities": New York: AIP Press; Springer, 2000.*

Eaton, J. A., Chromospheric emission of W Ursae Majoris-type stars and its relationto the structure of their common envelopes. 1983, *Astrophysical Journal*, **268**, 800, DOI: 10.1086/161002

Eaton, J. A., Odell, A. P., & Polakis, T. A., On the Period and Light Curve of the A-Type W UMa binary GSC 3208-1986. 2019, *Information Bulletin on Variable Stars*, **6263**, 1, DOI: 10.22444/IBVS.6263

Ekström, S., Georgy, C., Eggenberger, P., et al., Grids of stellar models with rotation. I. Models from 0.8 to 120 $M_\odot$ at solar metallicity (Z = 0.014). 2012, *Astronomy and Astrophysics*, **537**, A146, DOI: 10.1051/0004-6361/201117751

Gaia Collaboration, Brown, A. G. A., Vallenari, A., et al., Gaia Data Release 1. Summary of the astrometric, photometric, and survey properties. 2016, *Astronomy and Astrophysics*, **595**, A2, DOI: 10.1051/0004-6361/201629512

Gaia Collaboration, Vallenari, A., Brown, A. G. A., et al., Gaia Data Release 3. Summary of the content and survey properties. 2023, *Astronomy and Astrophysics*, **674**, A1, DOI: 10.1051/0004-6361/202243940

Gettel, S. J., Geske, M. T., & McKay, T. A., A Catalog of 1022 Bright Contact Binary Stars. 2006, *Astronomical Journal*, **131**, 621, DOI: 10.1086/498016

Girardi, L., Bressan, A., Bertelli, G., & Chiosi, C., Evolutionary tracks and isochrones for low- and intermediate-mass stars: From 0.15 to 7 M_{sun}, and from Z=0.0004 to 0.03. 2000, *Astronomy and Astrophysics, Supplement*, **141**, 371, DOI: 10.1051/aas:2000126

Harmanec, P., Stellar Masses and Radii Based on Modern Binary Data. 1988, *Bulletin of the Astronomical Institutes of Czechoslovakia*, **39**, 329

Hog, E., Kuzmin, A., Bastian, U., et al., The TYCHO Reference Catalogue. 1998, *Astronomy and Astrophysics*, **335**, L65

Kang, Y. W., Oh, K.-D., Kim, C.-H., et al., Period variation and spot model for the W UMa type binary TY UMa. 2002, *Monthly Notices of the RAS*, **331**, 707, DOI: 10.1046/j.1365-8711.2002.05246.x

Kopal, Z. 1959, *Close binary systems*

Liakos, A., Discovery of five W UMa systems. 2019, *Peremennye Zvezdy Prilozhenie*, **19**, 3

Liakos, A. & Niarchos, P., Observations of variables. 2011, *Information Bulletin on Variable Stars*, **5999**, 5

Lucy, L., Gravity-Darkening for Stars with Convective Envelopes. 1967, *Zeitschrift für Astrophysik*, **65**, 89.

Lucy, L. B., The Common Convective Envelope Model for W Ursae Majoris Systems and the Analysis of their Light Curves. 1973, *Astrophysics and Space Science*, **22**, 381, DOI: 10.1007/BF00647433

Malkov, O. Y., Mass-luminosity relation of intermediate-mass stars. 2007, *Monthly Notices of the RAS*, **382**, 1073, DOI: 10.1111/j.1365-2966.2007.12086.x

Milone, E. F., ed. 1993, *Light Curve Modeling of Eclipsing Binary Stars*

Paczyński, B., Szczygieł, D. M., Pilecki, B., & Pojmański, G., Eclipsing binaries in the All Sky Automated Survey catalogue. 2006, *Monthly Notices of the RAS*, **368**, 1311, DOI: 10.1111/j.1365-2966.2006.10223.x

Percy, J. R. 2007, *Understanding Variable Stars*

Popper, D., Stellar masses. 1980, *Ann. Rev. Astron. Astrophys.*, **18**, 115, DOI: 10.1146/annurev.aa.18.090180.000555

Ruciński, S. M., The Proximity Effects in Close Binary Systems. II. The Bolometric Reflection Effect for Stars with Deep Convective Envelopes. 1969, *Acta Astronomica*, **19**, 245

Samec, R. G., Kring, J. D., Robb, R., Van Hamme, W., & Faulkner, D. R., UBVRI Analysis of the Totally Eclipsing Extreme Mass Ratio W UMa Binary, GSC 3208 1986. 2015, *Astronomical Journal*, **149**, 90, DOI: 10.1088/0004-6256/149/3/90

van Hamme, W., New Limb-Darkening Coefficients for Modeling Binary Star Light Curves. 1993, *Astronomical Journal*, **106**, 2096, DOI: 10.1086/116788

Vilardell, F., Ribas, I., Jordi, C., Fitzpatrick, E. L., & Guinan, E. F., The distance to the Andromeda galaxy from eclipsing binaries. 2010, *Astronomy and Astrophysics*, **509**, A70, DOI: 10.1051/0004-6361/200913299

Wilson, R. E., Devinney, E. J., & Van Hamme, W. 2020, WD: Wilson-Devinney binary star modeling, Astrophysics Source Code Library, record ascl:2004.004

Woźniak, P. R., Vestrand, W. T., Akerlof, C. W., et al., Northern Sky Variability Survey: Public Data Release. 2004, *Astronomical Journal*, **127**, 2436, DOI: 10.1086/382719

The possible dual nature of the asteroid (12499) 1998 FR47

G. Borisov[1,2] , **N. Todorović**[3], **E. Vchkova-Bebekovska**[4],
A. Kostov[1] **and G. Apostolovska**[4]

[1] *Institute of Astronomy with NAO, Bulgarian Academy of Sciences, 72
Tsarigradsko Chaussée Blvd, BG-1784, Sofia, Bulgaria, (E-mail:
gborisov@astro.bas.bg)*

[2] *Armagh Observatory and Planetarium, College Hill, Armagh BT61 9DG,
Northern Ireland, United Kingdom*

[3] *Astronomical Observatory, Volgina 7, Belgrade, 11060, Serbia*

[4] *Institute of Physics, Ss. Cyril and Methodius University in Skopje, Faculty
of Natural Sciences and Mathematics-Skopje, Arhimedova 3, Skopje, 1000,
Republic of Macedonia*

Abstract. We present the R-band lightcurves of the Flora family asteroid
(12499) 1998 FR47, obtained in 2022 at two different astronomical sites: Bulgarian National Astronomical Observatory Rozhen (MPC Code 071) and Astronomical Station Vidojevica (MPC Code C89). The quadramodal lightcurves reveal a rotation period of 6.172±0.003 h and an amplitude of about 0.44 mag. Using the lightcurve inversion method, with the combination of our dense lightcurves and the sparse data from Gaia DR3, we found the sidereal period, an indication of a retrograde rotation of (12499) and its low-convex resolution shape. Nonetheless, the unusual shape of the quadramodal lightcurve and its additional analysis reveals two possible periods, 3.0834±0.0085 h and 4.1245±0.0151 h, making the suspect that the asteroid might be a non-synchronised wide binary system. Spectral analysis of the asteroid using data from the GAIA DR3 shows that it is either an M- or an L-type object and maybe a piece of the first planetesimals to form in the Solar System protoplanetary disk. On the other hand, (12499)'s dynamical properties indicate a significantly shorter lifetime. The asteroid lies exactly on the chaotic border of the 7:4 mean motion resonance with Mars (7M:4), alternating between being in and out of it for almost 190 Myrs. During 200 Myrs of integration, (12499) visited other resonances in the Flora family, but it never became a Near Earth Object (NEO). Additional integration of fictive objects from the 7M:4 resonance showed a possibility of transportation to the NEO region already at about 20 Myrs.

Key words: binary asteroid – (12499) 1998 FR47 – photometry – spectroscopy

1. Introduction

An asteroid lightcurve is constructed by the rotation of an irregular ellipsoidal shape. In the usual case, lightcurves during one rotational phase should have two maxima and two minima with slightly different depths. On the other hand, some asteroids have shown unusual lightcurve shapes, which may be caused by different albedo over their surfaces or irregular shapes. Lately, different observational techniques confirm that some of these irregular lightcurves shapes could be caused by the binary nature of the observed asteroids (Tedesco, 1979; Margot et al., 2015). In the last two decades, numerous studies of these asteroid binary systems have been done, and the estimation is that around 15 % of the Near Earth Asteroids (NEA's), with diameters greater than 0.3 km, belong to this class (Pravec et al., 2006). There are a few characteristics of the lightcurve that may suggest the possibility of a binary system. The most common one is the presence of two minima with different depths separated by a half phase, which is usually caused by mutual events like occultations and eclipses between the two components. Unfortunately, determining a binary system is not always straightforward. If the system is not positioned equatorially to the observer or the components of the binary are distinctly separated, these features will not be presented in the lightcurve.

The asteroid (12499) 1998 FR47 was discovered on 1998 March 20 by the LINEAR project in Soccoro (New Mexico, USA). According to the Asteroid Lightcurve Photometry Database (ALCDEF)[1] (Stephens & Warner, 2018; Warner et al., 2009), the calculated diameter of (12499) is 4.591 km, and the assumed albedo is 0.277 (Mainzer et al., 2019). A search of the Asteroid Lightcurve Database found no previously reported period for asteroid (12499). The only available information about the asteroid lightcurve was its amplitude of 0.4 mag, reported by Simpson et al. (2013).

The asteroid (12499) is located at about 2.21 AU in the inner main belt in the region of the Flora family (although its membership to the family is somewhat questionable). According to Nesvorny (2020) it belongs to the Flora family, while the AstDys database[2] denoted it as a background asteroid. This discrepancy can be explained by the fact that the Flora family does not have sharp boundaries, but it gradually fades into the background population (see e.g. Vokrouhlický et al. (2017); Dykhuis et al. (2014)). Nevertheless, here we study only one of its potential members in the same way we studied the asteroid (4940) Polenov (Vchkova Bebekovska et al., 2021).

[1]https://alcdef.org

[2]Available at https://newton.spacedys.com/astdys/

2. Observations and data reduction

Our first photometric observations of the asteroid (12499) 1998 FR47 were on 2022 Aug 18 and 19, at Bulgarian National Astronomical Observatory (BNAO) Rozhen (MPC Code 071), when our primary targets were long-term studied asteroids. The observations were performed with a 50/70 Schmidt telescope, equipped with an FLI PL 16803 4096×24096 CCD with 9 μm pixels. The next observations were conducted on 2022 Sep 23 and 24 at Astronomical Station (AS) Vidojevica (MPC Code C89) with 60 cm Cassegrain "Nedeljković" telescopes equipped with an SBIG STXL-6303 3072×2047 CCD with 9 μm pixels.

After light image reduction, aperture photometry of the asteroid and comparison stars were performed with the software program CCDPHOT[3] by Buie (1996). For the lightcurve analysis, we used the software package MPO Canopus v10.8.4.1 [4], which produces composite lightcurves, calculates rotational periods, provides the Fourier analysis fitting procedure, and estimates the amplitude of the lightcurve.

Table 1 presents the aspect data for (12499) for the observational sets and Fig. 1 shows the Phase Angle Bisector (PAB) longitude, PAB latitude, and phase angle distributions for dense and sparse photometric data. Dense data correspond to observations in Table 1 and sparse data correspond to 19 accurate photometric points from 31 December 2014 to 13 May 2017 from GAIA Data Release 3 (DR3). The phase angles of the sparse satellite data are between 19 and 32 degrees and the phase angles of our dense data fill the gap around the asteroid opposition.
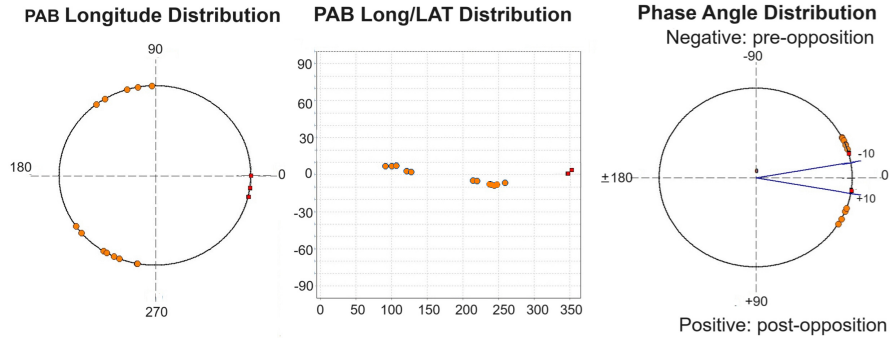
Figure 1. Dense (red points) and Gaia DR3 sparse observations (orange points). Left: Distribution of PAB longitude; Centre: Distribution of PAB longitude on PAB latitude; Right: Distribution of phase angle.

---

[3]https://www.boulder.swri.edu/~buie/idl/ccdphot.html

[4]https://minplanobs.org/BdwPub/php/mpocanopus.php

Table 1. Aspect data for the asteroid (12499) 1998 FR47 for the five observational sets.

Date[1] (UT)	r[2] (AU)	Δ[3] (AU)	Ph. angle[4] ($\alpha°$)	λ_e[5] (°)	β_e[6] (°)	MPC[7] code
2022 Aug 19.02	1.707	0.747	16.7016	355.04	0.26	071
2022 Aug 20.01	1.707	0.746	16.1411	354.96	0.40	071
2022 Sep 23.99	1.713	0.721	7.6643	348.70	5.12	C89
2022 Sep 24.04	1.713	0.721	7.7522	348.67	5.14	C89
2022 Sep 24.83	1.714	0.724	8.2522	348.53	5.22	C89

[1] The observation date referring to the mid-time of the lightcurve observed
[2] Heliocentric distance
[3] Geocentric distance
[4] The solar phase angle
[5] The J2000.0 ecliptic longitude
[6] The J2000.0 ecliptic latitude
[7] Minor Planet Centre Observatory Code
https://www.minorplanetcenter.net/iau/lists/ObsCodesF.html

3. Results

3.1. Lightcurve analysis

During the first night (12499) was observed for about 2.8 hours. By visual inspection of the typical asteroid bimodal symmetrical lightcurve, we thought that more than 90 % of its period was covered. To our surprise, the next night's observations with a duration of 4.5 h showed an asymmetrical lightcurve having three minima with different amplitudes. Combining these two nights' observations, we could not determine the rotational period.

During the next observations, carried out at AS Vidojevica, Sep 23 and 24, 2022, the solar phase angle of the asteroid was at 7.8° after opposition, and the asteroid was observed for about 8 and 4 hours, respectively. A Fourier fit of order 9 reveals an asymmetric quadramodal shape of the composite lightcurve and confirms a period of 6.172±0.003 h with an amplitude of 0.44±0.01 mag (see Fig. 2). Using the empirical relation between the amplitude and largest to the smallest axis ratio (a/c) proposed by Zappala et al. (1990) we computed a/c=1.39. Four well-defined maxima and minima with different heights could be due to an irregular shape of the asteroid and/or albedo variations on its surface.

This period was used in constructing the composite lightcurve from the previous observations, which were taken at a phase angle of 16.7° before opposition.
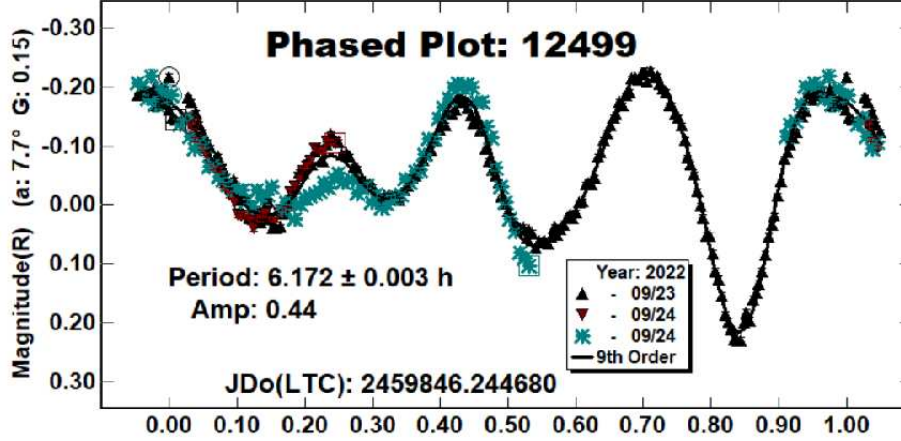
Figure 2. The composite lightcurve of (12499) 1998 FR47 gathered from the observations on 23 and 24 September 2020. The Fourier analysis of order 9 gave the best corresponding to the rotational period 6.172h±0.003 h with the amplitude of 0.44±0.01 mag.

Even though the data have a gap, the composite lightcurve constructed with a Fourier fit of order 6 again reveals an asymmetric quadramodal shape, that looks like a mirror image of the first composite lightcurve (see Fig. 3).

3.2. Testing a single-body shape model

Even though the irregular form of the observed lightcurve we decided to test for a single-body low-resolution shape model. For this purpose, we used the lightcurve inversion method (Kaasalainen & Torppa, 2001; Kaasalainen et al., 2001) and LCInvert programme part of the MPO Software[5]. Considering the tremendous accuracy of the DR3 photometric data we took the weighting factor to be set to 1.0 for both sparse and for dense photometric data. These sparse data added to our dense data give us a wide range of the PAB longitude distribution (see Fig. 1) which is very important for the shape reconstruction. We made the initial sidereal period search around our synodic period of 6.172 h (see Fig. 4–left panel). A narrower period search found a few solutions with 10 % of the lowest χ^2 (see Fig. 4–right panel), but we choose the one with the lowest χ^2, which is 6.16802461 h, as the most likely period and used it for the pole search.

The pole search produced 312 discrete and fixed pole positions distributed over the unit sphere with 15° steps in ecliptic latitude and longitude. The dark blue region in the constructed χ^2-map, presented in Fig. 5, has χ^2-value about

---

[5]https://minplanobs.org/BdwPub/php/displayhome.php
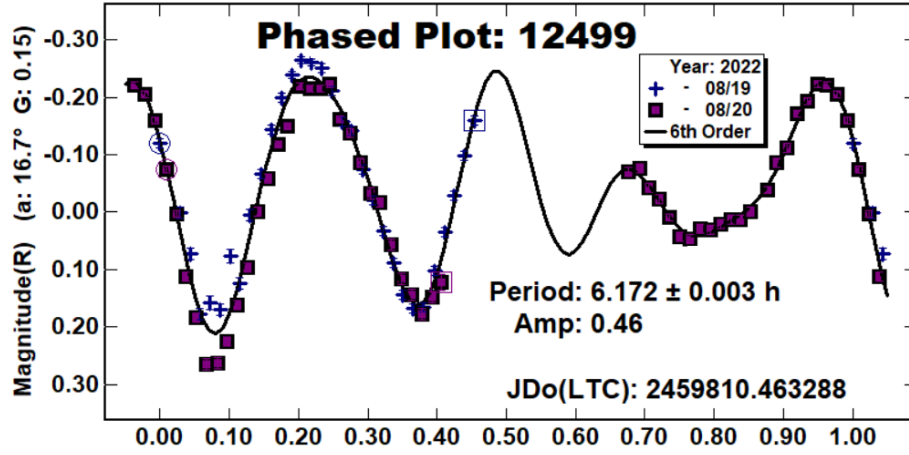
Figure 3. The lightcurve of (12499) 1998 FR47 gathered from the observations in August 2022. Although not completely covered, it is constructed on the basis of the afterwards calculated period of 6.172 h.
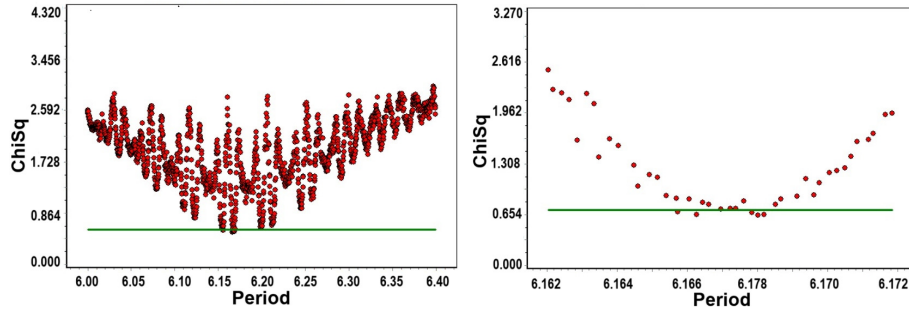
Figure 4. The periodograms of the initial sidereal period search around our synodic period of 6.172 h.

25 % smaller than χ^2-values of the dark red region. It corresponds to pole co-ordinates λ=300° and β=-60° and sidereal period 6.168027718 h. Taking those values as free parameters we made a finer pole search and we got sidereal period 6.16799606 h and pole coordinates λ=291.9° and β=-53.2°, which suggest the retrograde sense of the asteroid rotation. Assuming the triaxial ellipsoid form of the asteroid with axes a>b>c, which rotates around the shortest axis c=1, the calculated pole coordinates corresponded to the relative shape dimensions a/b=1.1 and a/c=1.3. The corresponding 3D shape model is also constructed and presented in Fig. 6. The comparison of the lightcurves generated from this

model with the dense lightcurves is shown in Fig.7. The modelled lightcurves in Fig.7 do not correspond well enough with the observations. These, together with the initial irregular form of the observed lightcurve, were indicators for searching for a double-period solution caused by the binary nature of the asteroid.
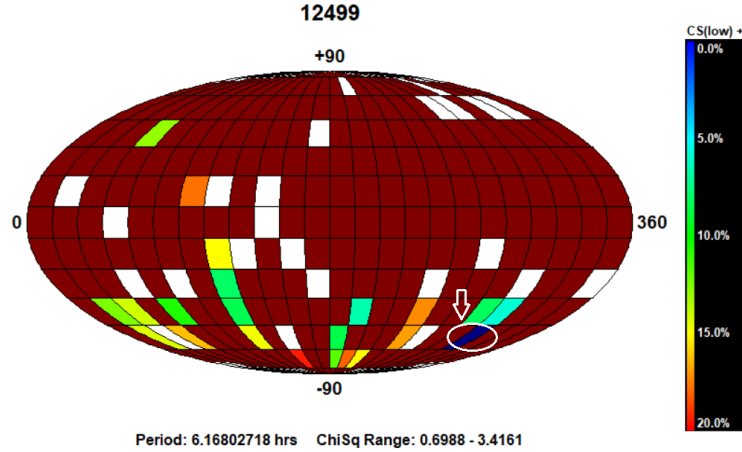

Figure 5. The χ^2-map of the pole search distribution. The white arrows indicate the dark blue region with the smallest value of χ^2. The dark blue regions have χ^2 values about 20% smaller than χ^2 values of the dark red regions.

3.3. Possible binary system

The complex form of the lightcurves, the unusual depth of one of the minima, as well as the diameter of the asteroid (smaller than 10 km), suggest that there could be two additive components in the lightcurve and that (12499) could be a candidate for a binary asteroid (Pravec et al., 2019). Using a Dual-period search (Warner, 2016) in MPO Canopus, we calculated the rotational period of the synodic period of both components. The first one has a period of 3.0834±0.0085 h and an amplitude of 0.27 mag and is presented in Fig. 8. The second one is with a period of 4.1245±0.0151 h and an amplitude of 0.22 mag and is presented in Fig. 9. Unfortunately, our observations did not capture any superimposed mutual events, and the distance between the two bodies is not constrained. The orbital period of the satellite using the data from these events could not be determined, which suggests that it may be a wide binary system.

Additional data from our observations and data from observers sufficiently far away in longitude are needed to cover the orbital period with mutual events (i.e. occultations and/or eclipses). It will help not only to decide if (12499) is a binary asteroid but also to refine our calculated periods for the primary and
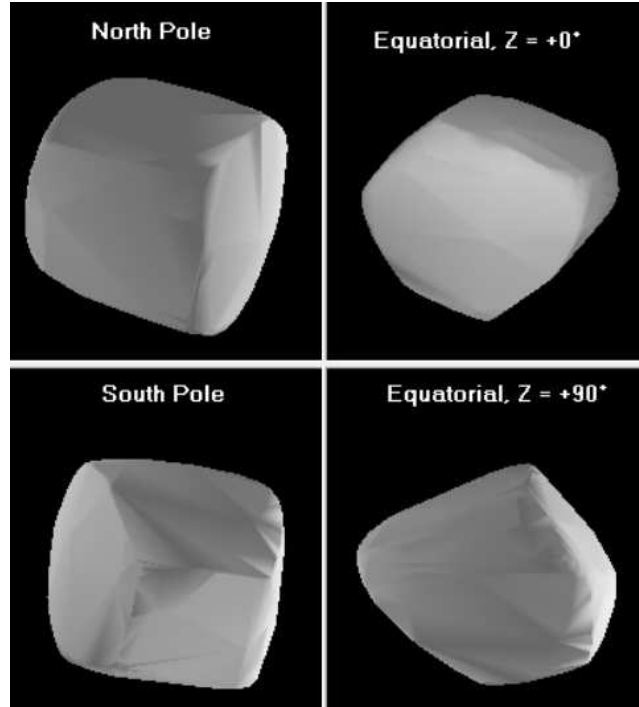
Figure 6. The 3D low-resolution convex shape model of (12499) 1998 FR47. The north and south pole views are given in two left panels, while the equatorial viewings with rotational phases 90° apart are given in two right panels. The calculated aspect ratio of the longest to two shorter semi-axis is a/b=1.1 and a/c=1.3.

for the secondary, as well as to determine the orbital period of the system. The best way is to organise an observational campaign on this object in the future.

3.4. Taxonomy from Gaia spectroscopy

The Gaia mission has been observing Solar System objects since the beginning of its operation. The Gaia DR3 includes, for the first time, the mean reflectance spectra of selected asteroids. Considering that (12499) is among them, we will use that data to further investigate its properties in the direction of taxonomy and composition, relying on the new probabilistic approach by Mahlke et al. (2022).

The results are shown in Fig. 10. The left panel shows the Gaia DR3 reflectance spectra of the object, the middle panel points out its latest published albedo obtained by NEOWISE (Mainzer et al., 2019), and the right panel presents the possible taxonomy classes with their probabilities.
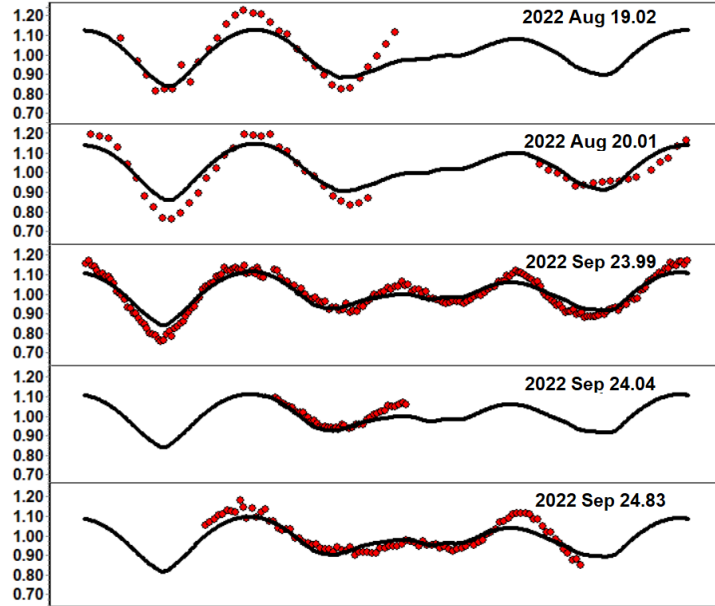
Figure 7. The lightcurve (red points) obtained from our dense observations superimposed over the lightcurves generated by the model constructed using a combination of our dense and GAIA DR3 sparse data.

In particular, the asteroid has a 66 % probability of being an M-class object and 30 % for an L-class. Both of these solutions fall into very diverse classes situated between primitive carbonaceous C- and silicate (partially thermally metamorphosed) S-classes (Cloutis et al., 1990, 2011; Vernazza et al., 2014). Other low probability solutions are 3 % for being an S-type object and 1 % for E-type.

The most probable M-class, which according to Mahlke et al. (2022) corresponds to the old Tholen (1984) M-class or the newest Bus-DeMeo (Bus & Binzel, 2002; DeMeo et al., 2009) Xk-class. Its reflectance spectrum has a linear red slope and possible faint features around $0.9\,\mu$m. The objects of this class are associated with at least two populations, the chondritic and the metallic (Vernazza et al., 2011; Viikinkoski et al., 2017), whose composition can vary, depending on their distance from the Sun and the time of format. The most probable formation scenario for M-type objects is that they are formed from a differentiated parent body after a collision and the fragments from the core, which were rich in metals, were formed them.

On the other hand, the reflectance spectrum of L-class asteroids is variable apart from a red visible slope and a small feature around $1\,\mu$m (Sunshine et al.,
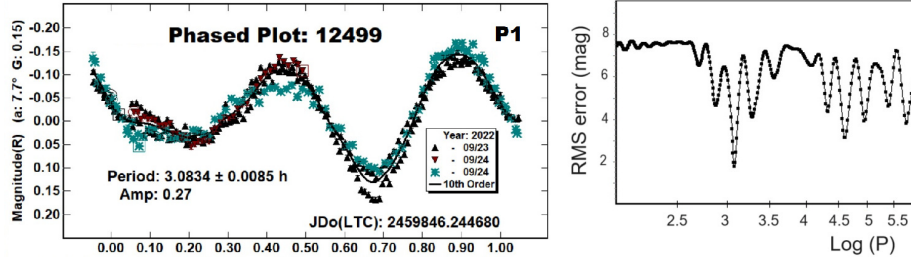
Figure 8. (12499) 1998 FR47 – the lightcurve of the primary (left panel) and the corresponding dual-period search periodogram (right panel).
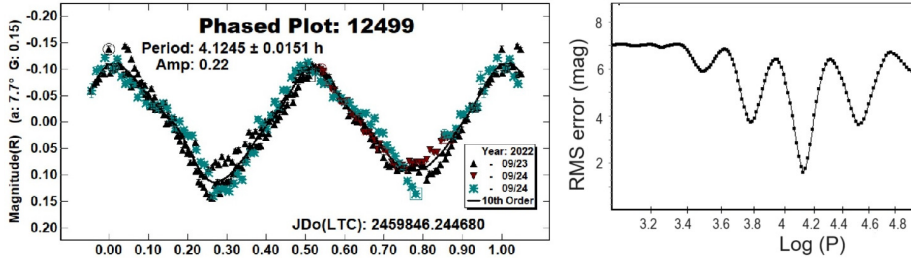

Figure 9. (12499) 1998 FR47 – the lightcurve of the secondary (left panel) and the corresponding dual-period search periodogram (right panel).

2008). The composition of this type of object is associated with large abundances of spinelbearing calcium–aluminium-rich inclusions, suggesting they may be pieces of the first planetesimals to form in the Solar System's protoplanetary disk (Devogèle et al., 2018).

3.5. Dynamical properties

Let us first remark that (12499)'s membership to the Flora family indirectly suggests that (12499) could be stable in long times, since the age of the family is estimated to $\sim 1\,\mathrm{Gyr}$ (Hanuš et al., 2013; Dykhuis et al., 2014; Brož et al., 2013). We will verify these stability assumptions in two ways: (a) by mapping and studying the orbital neighbourhood of the asteroid (b) by tracking the evolution of (12499) and several fictive objects in its close neighbourhood.

The calculation of maps is performed using the Fast Lyapunov Indicator - FLI (Froeschlé et al., 1997), a numerical tool which is efficient in dynamical cartography of both realistic (Daquin et al., 2016, 2022; Rosengren et al., 2017; Todorović, 2020, 2017) and idealised systems (Froeschlé et al., 2000). FLI values and the orbital evolution of individual test particles (TPs) are obtained
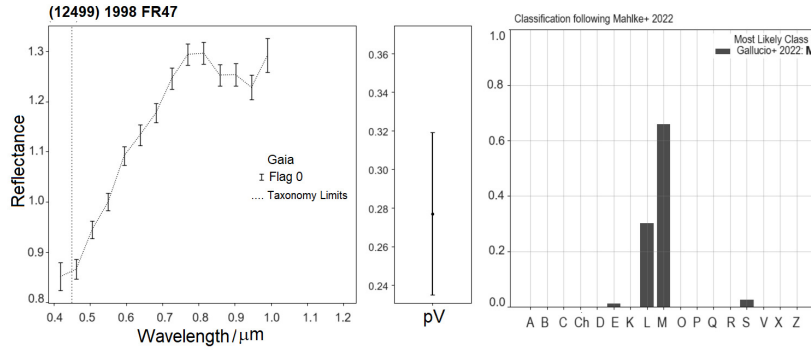
Figure 10. Gaia DR3 reflectance spectrum of (12499) 1998 FR47 and its taxonomical classification according to Mahlke et al. (2022) (see text for details).

with the orbit9 integrator available at http://adams.dm.unipi.it/orbfit/. We consider the gravitational influences of seven planets from Venus to Neptune. The mass of Mercury is added to the mass of the Sun, and a proper barycentric correction is applied. The non-gravitational Yarkovsky and YORP effects are not included in the calculation. In the integration, asteroids are treated as massless test particles. We do not consider their sense of rotation, nor the eventual mutual gravitational effect of the components in the possible binary system.

Fig. 11 shows one segment of the semi-major axis eccentricity (a, e) plane around the asteroid (12499). It is produced by taking 250 000 TPs regularly distributed on a 500 x 500 grid in $[a, e] = [2.18, 2.24] \times [0.15, 0.35]$. For each TP we calculate its corresponding FLI for 5000 years. Stable orbits have lower FLIs and are marked with dark blue colours, while the more chaotic ones have higher FLIs and are coloured with lighter shades of blue. The four remaining orbital elements, the inclination i, the longitude of the node Ω, the argument of the pericentre ω, and the mean anomaly M, are equal to the corresponding elements of (12499) for the epoch 2458800.5 MJD (13. November 2019). Their values are taken from the JPL NASA database[6] and are approximately $(i, \Omega, \omega, M) \sim (6.76°, 337.11°, 6.71°, 53.79°)$. By using this mapping method, we can see the realistic dynamical environment of (12499).

The map in Fig. 11 shows a large number of mean motion resonances (MMRs) appearing as vertical thin V-shaped structures. Additional calculations (not shown here) verified that most of them are resonances with Mars, confirming the domination of such resonances in the Flora family (Vokrouhlický et al., 2017; Nesvorný et al., 2002).

The location of the asteroid (12499) at $(a, e) = (2.21209, 0.23150)$ is marked with a white dot, while the green diamond shape at $(a, e) = (2.18289, 0.15945)$

---

[6]Available at https://ssd.jpl.nasa.gov/
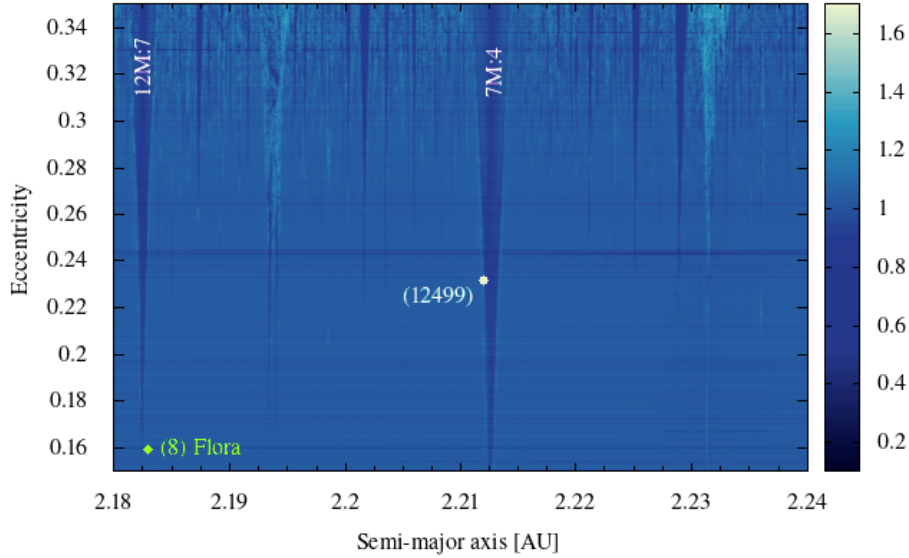
Figure 11. The 5000 years FLI map calculated in the semi-major axis, eccentricity plane for $[a, e] = [2.18, 2.24] \times [0.15, 0.35]$, where most of the vertical V-shaped structures are mean motion resonances with Mars. The asteroid (12499), marked with a white dot, lies close to the 7M:4 MMR at $a \sim 2.212$ AU. The position of the asteroid (8) Flora, the largest body in the family, is marked with a green diamond-like shape close to the 12M:7 MMR at about $a \sim 2.182$ AU.

shows the position of the asteroid (8) Flora, the possible largest remnant of the parent body of the family. Although our paper focuses on the asteroid (12499), we will make some other remarks on Fig. 11. Vokrouhlický et al. (2017) showed that the asteroid (8) Flora is close to the ν_6 and ν_{16} secular resonances[7]. Their presence is not visible on our map since it would require much longer integration times than 5000 yrs used here (see Todorović & Novaković (2015) for the detection of secular resonance in FLI maps). In Fig. 11 it appears that (8) Flora is close to the 12:7 MMR with Mars at about $a \sim 2.182$ AU (for the identification of mean motion resonances see e.g. Gallardo (2006); Smirnov (2023)). Still, its exact distance from the 12M:7 resonance as visible on the chart, is not entirely reliable, since the map illustrates the dynamical situa-

---

[7]Resonances ν_6 and ν_{16} occur when the precession and nodal frequencies of the asteroid's orbit equal the precession and nodal frequencies of the orbit of Saturn, respectively.
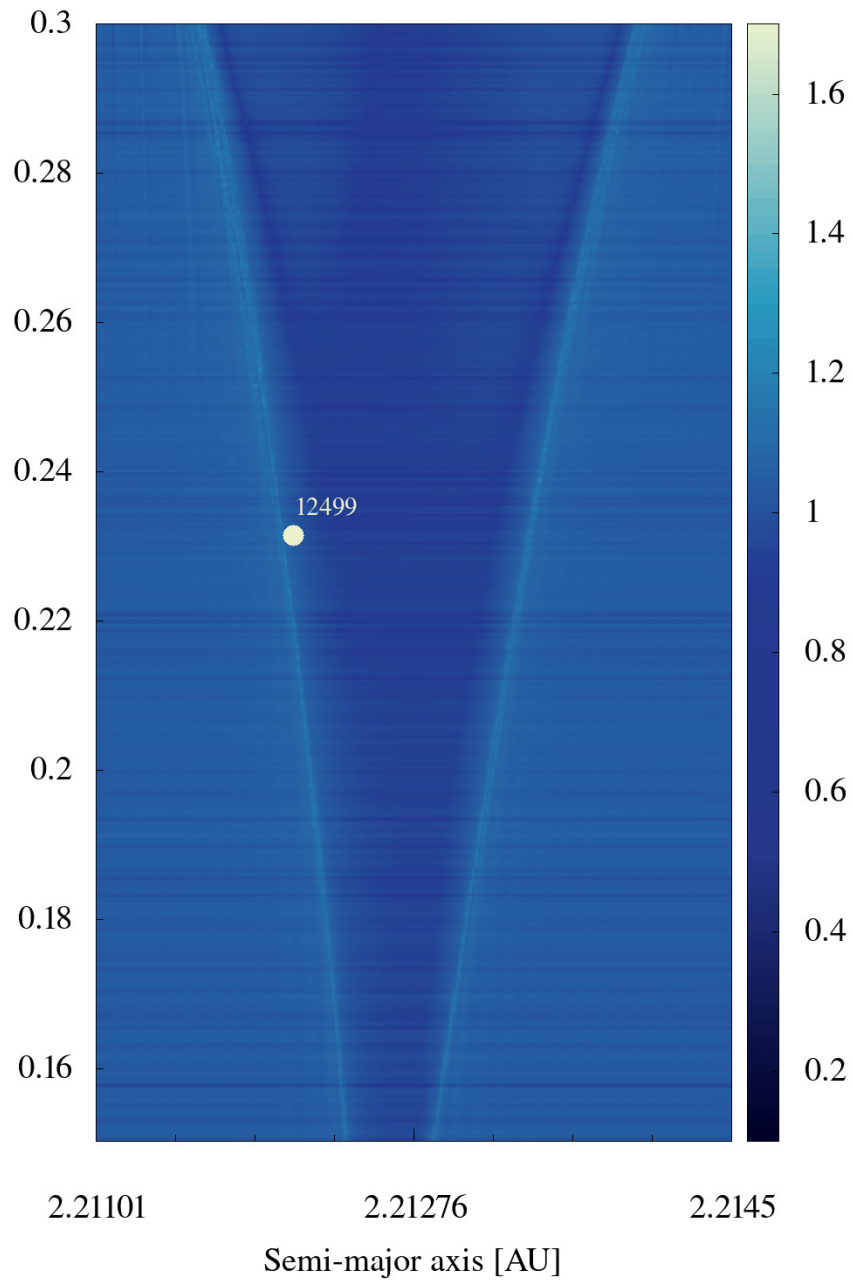
tion in the orbital plane of the asteroid (12499). The shape and the positions of resonances change with the change of orbital angles, and according to the JPL database for the particular epoch, (8) Flora is 199.6 degrees in front of (12499) in the mean anomaly M, it has 226.2 degrees larger longitude of the node Ω, and is 79.6 degrees behind in the argument of pericentre ω, id est $M_{(8)} - M_{(12499)} = 199.6°, \Omega_{(8)} - \Omega_{(12499)} = 226.2°, \omega_{(8)} - \omega_{(12499)} = -79.6°$.

In Fig. 11 the asteroid (12499) is placed at the 7:4 mean motion resonance with Mars. In a closer look given in Fig. 12, for $[a, e] = [2.21101, 2.2145] \times [0.15, 0.3]$, we notice that (12499) lies exactly on the chaotic border of the resonance.

Several asteroid pairs are already associated with mean motion resonances (see for example Pravec et al. (2019), Duddy et al. (2012), or Rosaev (2024)). We are unaware that any such pair is found on the very edge of resonance, as is the case for (12499). It remains an open question whether the position on the resonant border may be related to the duality (binarity) of the asteroid.

In the following part, we will verify the long-term stability of (12499). In Fig. 13 we show two perspectives of its orbital evolution during 200 Myrs. The top panel shows which parts of the (a, e) plane are visited by (12499), where its trace is coloured pink. The lower panel gives the change of (12499)'s semi-major axis $a_{(12499)}$ during the integration time. The value of $a_{(12499)}$ remains close to the centre of the 7M:4 resonance at ~ 2.212 AU for about 190 Myrs, after which it starts an excursion to nearby resonances, but inside the family. We use the rough boundaries of the Flora family from Nesvorný et al. (2002) which are $2.12 < a < 2.31$ AU, $0.11 < e < 0.175$, and $3 < i < 7.5°$. The (12499)'s perihelion distance q reached Mars crossing values ($q = 1.665$ AU) several times, for the first time after about 0.6 Myrs. However, (12499) did not become a Near Earth Object ($q < 1.3$ AU) since its minimal perihelion distance was about $q \sim 1.4$ AU.

Another look at (12499)'s evolution for $t \in [50, 155]$ Kyrs is given in Fig. 14. On the top plot, we track the critical angle of (12499) for the 7M:4 resonance defined with $\sigma_{7M:4} = 7\lambda_a + 4\lambda_M - 3\tilde{\omega}_a$, where λ_a and λ_M are the mean longitudes of the asteroid and Mars respectively, (defined with $\lambda = M + \omega + \Omega$), while $\tilde{\omega}_a$ is the asteroids longitude of perihelion $\tilde{\omega} = \omega + \Omega$. The lower panel shows the evolution of $a_{(12499)}$ for the same time. We notice that $\sigma_{7M:4}$ and $a_{(12499)}$ have synchronised changes. In the first 80 Kyrs, $\sigma_{7M:4}$ librates, and $a_{(12499)}$ oscillates, meaning the asteroid is trapped in the resonance. In the next 70 Kyrs the asteroid is outside the resonance since the critical angle circulates (it has smooth changes in the $[0, 360]$ interval), while $a_{(12499)}$ is almost constant. The next entry in the 7M:4 resonance starts at ~ 130 Kyrs and lasts for about 20 Kyrs. Such alternating episodes of going in and out of the resonance are observed for 190 Myrs. In Fig. 14 we plotted a relatively short time interval of about ~ 100 Kyrs (between $t \in [50, 155]$ Kyrs), because the fine oscillations in $\sigma_{7M:4}$ and $a_{(12499)}$ are not noticeable for a 200 Myrs interval (see panel b in Fig. 13).

Figure 12. The enlarged portion of Fig. 11 around the 7M:4 resonance for $[a, e] = [2.21101, 2.2145]$ AU $\times [0.15, 0.3]$. The asteroid (12499), marked with the white dot, is located exactly on the chaotic border of the resonance.
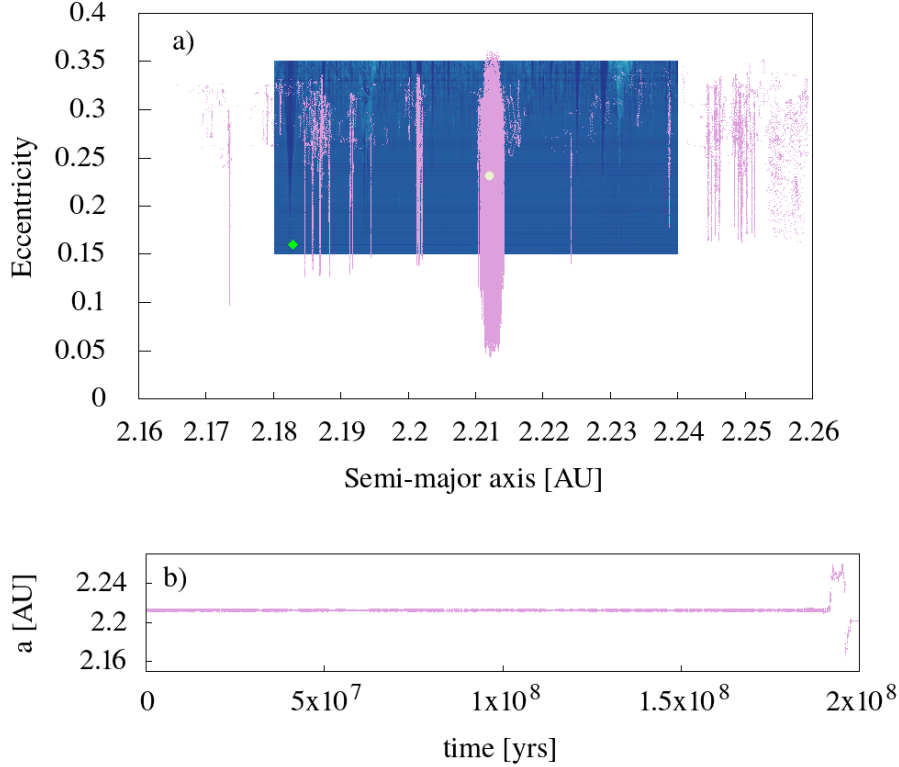
Figure 13. The top panel shows the orbital evolution of (12499) in the (a, e) plane during 200 Myrs of integration. The places visited by the asteroid are coloured pink. The map from Fig. 11 is set in the background for better orientation. In addition to the 7M:4 resonance at $a \sim 2.212$ AU (from which it originated), (12499) visited numerous neighbouring resonances but did not leave the Flora family. The lower panel shows the evolution of $a_{(12499)}$ during the whole integration time. The asteroid remains close to (or inside) the 7M:4 resonance at $a \sim 2.212$ AU for almost 190 Myrs. Its excursion to the neighbouring MMRs occurred in the last 10 Myrs of integration.

In the end, we selected 20 additional TPs from the chaotic border of the 7M:4 MMR from Fig. 12 and observed their orbital evolution in 50 Myrs. Assuming (12499) could be a binary asteroid lying on the chaotic border of a resonance, we may expect that initially close segments could have a large orbital divergence. We emphasise again that we did not treat the gravitational interaction between the possible components of the binary, but only the evolution of individual massless TPs in the above-described Solar system model.
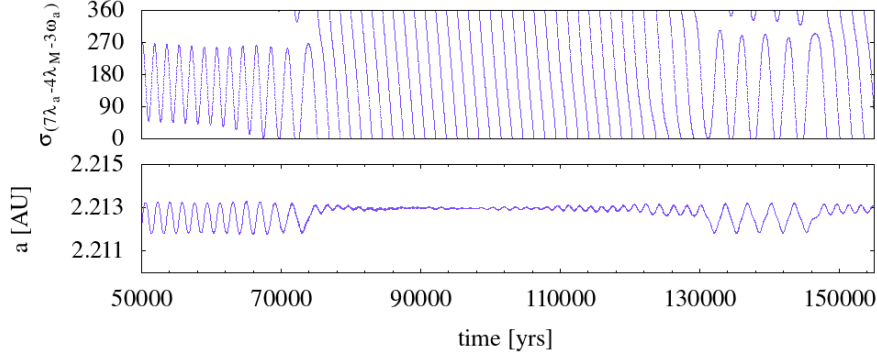
Figure 14. The change of (12499)'s critical angle for the 7M:4 MMR $\sigma_{7M:4}$ (top panel) and the change of its semi-major axis $a_{(12499)}$ (bottom panel) for $t \in [50, 155]$ Kyrs. The asteroid spent around 72 Kyrs librating in the resonance (the first 50 Kyrs are not presented). In the next 80 Kyrs i.e. until ~ 130 Kyrs, $\sigma_{7M:4}$ circulates, meaning the asteroid was pushed out of the resonance, but not far since its semi-major axis has a quasi-constant value close to the resonance at about $a_{(12499)} \sim 2.213 \, AU$. Another episode of libration in $\sigma_{7M:4}$ and oscillation in $a_{(12499)}$ occurred between 130 and 150 Kyrs, meaning the asteroid is trapped in the resonance again. We observed that such libration-oscillation modes in $\sigma_{7M:4}$ alternate for about 190 million years.

The results of this last set of integration are given in Fig. 15. Again, we show the (a, e) plane but for a larger domain for $[a, e] = [0, 100]$AU $\times [0, 1]$, where the semi-major axis is presented on the logarithmic scale. This portion of the (a, e) plane was selected because we observed large-scale changes in the orbital elements of the test asteroids. More precisely, 4 among the 20 objects experienced macroscopic evolution through the Solar system. These four asteroids were thrown out of the resonance by close approaches with Mars, followed by a series of encounters with Earth and Venus. Only one among the four test objects had an approach with Jupiter. The resulting orbital pathways in the (a, e) plane are coloured in red (Fig. 15). We notice they spread mostly between the apsidal lines of Jupiter q_J and Q_J (marked with two grey lines). The first entries in the NEO region are observed at about 20 Myrs, in significantly shorter times than the average deliveries of 100 Myrs as reported in Nesvorný et al. (2002). The remaining 16 test asteroids stayed in the 7M:4 resonance; their trace in the chart at about 2.21 AU, is coloured green. Let us mention that this result represents a possible outcome of the chaotic evolution, whereas, in reality, we could expect shorter evolution timescales, due to eventual close approaches with the largest asteroids and/or nongravitational effects like YORP and Yarkovsky.

Our results show that the Flora family is efficient in supplying the NEO region also through weak MMRs with Mars, not only via the ν_6 resonance as a

main driver. Still, we emphasise that this last set of test asteroids is intentionally chosen from the resonant chaotic border, meaning the real possibilities for this scenario are somewhat lower, but not impossible.
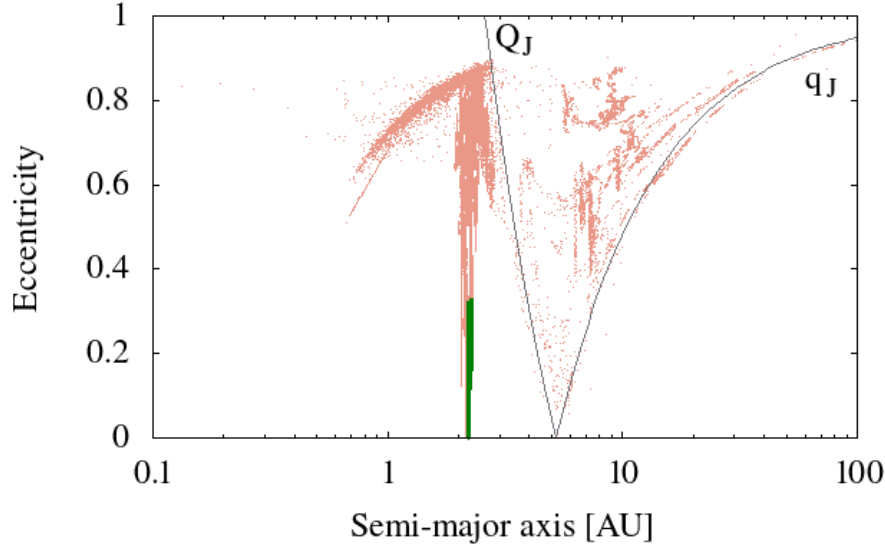
Figure 15. The trace of 20 test asteroids initially placed on the borders of the 7:4 MMR with Mars, during 50 Myrs of orbital evolution. We cover a large segment of the Solar system $[a, e] = [0, 100]\,\mathrm{AU} \times [0, 1]$, where the semi-major axis is given in the $\log_{10}$ scale. Among the 20 test objects, four of them were thrown out of resonance due to close approaches with Mars (and other inner planets), entered the NEO region and experienced a macroscopic diffusion through the Solar system (their traces are coloured red). The 16 remaining bodies stayed close to the 7M:4 MMR around $a \sim 2.212\,\mathrm{AU}$. Their trace in the chart is coloured green. The two apsidal lines of Jupiter q_J and Q_J are marked with thin light grey lines.

4. Conclusions

The unusual shape of the observed lightcurve for the asteroid (12499) 1998 FR47 was investigated in different senses. Firstly we try to determine the rotational period, axis poles, and shape of the object assuming a single body. The

solution suggests a rare quadramodal shape of the lightcurve with a rotational period of 6.172±0.003 h and an unusual shape to model it. Then we saw that the lightcurve can be modelled by two different periods and performed a dual-period search assuming that the asteroid is a binary system. The two solutions are 3.0834±0.0085 h and 4.1245±0.0151 h respectively for the primary and secondary bodies. No mutual event was detected in the lightcurve, so we suppose that these periods are of the individual lightcurves of the two bodies of the system, which is not synchronised and most probably is a wide binary system.

The available Gaia DR3 reflectance spectrum of the object suggests either M- or L-type taxonomy. They both are from the M-complex and suggest either chondritic or metallic composition or an object with large abundances of spinelbearing calcium–aluminium-rich inclusions, suggesting that the asteroid (12499) might be a piece of the first planetesimals to form in the Solar System protoplanetary disk.

Dynamical studies showed that (12499) is located at the very edge of the 7:4 mean motion resonance with Mars, where it should spend the next 190 Myrs, after which it should start a tour of nearby resonances. Additional calculations showed that TPs on the chaotic border of the 7M:4 MMR, close to (12499), may experience shorter stays in the resonance and faster deliveries to the NEO region and/or macroscopic diffusion starting already at 20 Myrs. Since our model does not include Yarkovsky or YORP effects, there is a possibility that the reported times are even shorter.

References

Brož, M., Morbidelli, A., Bottke, W. F., et al., Constraining the cometary flux through the asteroid belt during the late heavy bombardment. 2013, *Astronomy and Astrophysics*, **551**, A117, DOI: 10.1051/0004-6361/201219296

Buie, M. W., CCDPHOT—An IDL Widget Based CCD Photometry Reduction System. 1996, in Astronomical Society of the Pacific Conference Series, Vol. **101**, *Astronomical Data Analysis Software and Systems V*, ed. G. H. Jacoby & J. Barnes, 135

Bus, S. J. & Binzel, R. P., Phase II of the Small Main-Belt Asteroid Spectroscopic Survey. A Feature-Based Taxonomy. 2002, *Icarus*, **158**, 146, DOI: 10.1006/icar.2002.6856

Cloutis, E. A., Gaffey, M. J., Smith, D. G. W., & Lambert, R. S. J., Metal Silicate Mixtures: Spectral Properties and Applications to Asteroid Taxonomy. 1990, *Journal of Geophysics Research*, **95**, 8323, DOI: 10.1029/JB095iB06p08323

Cloutis, E. A., Hudon, P., Hiroi, T., Gaffey, M. J., & Mann, P., Spectral reflectance properties of carbonaceous chondrites: 2. CM chondrites. 2011, *Icarus*, **216**, 309, DOI: 10.1016/j.icarus.2011.09.009

Daquin, J., Legnaro, E., Gkolias, I., & Efthymiopoulos, C., A deep dive into the 2 g +h resonance: separatrices, manifolds and phase space structure of navigation satellites. 2022, *Celestial Mechanics and Dynamical Astronomy*, **134**, 6, DOI: 10.1007/s10569-021-10060-6

Daquin, J., Rosengren, A. J., Alessi, E. M., et al., The dynamical structure of the MEO region: long-term stability, chaos, and transport. 2016, *Celestial Mechanics and Dynamical Astronomy*, **124**, 335, DOI: 10.1007/s10569-015-9665-9

DeMeo, F. E., Binzel, R. P., Slivan, S. M., & Bus, S. J., An extension of the Bus asteroid taxonomy into the near-infrared. 2009, *Icarus*, **202**, 160, DOI: 10.1016/j.icarus.2009.02.005

Devogèle, M., Tanga, P., Cellino, A., et al., New polarimetric and spectroscopic evidence of anomalous enrichment in spinel-bearing calcium-aluminium-rich inclusions among L-type asteroids. 2018, *Icarus*, **304**, 31, DOI: 10.1016/j.icarus.2017.12.026

Duddy, S. R., Lowry, S. C., Wolters, S. D., et al., Physical and dynamical characterisation of the unbound asteroid pair 7343-154634. 2012, *Astronomy and Astrophysics*, **539**, A36, DOI: 10.1051/0004-6361/201118302

Dykhuis, M. J., Molnar, L., Van Kooten, S. J., & Greenberg, R., Defining the Flora Family: Orbital properties, reflectance properties and age. 2014, *Icarus*, **243**, 111, DOI: 10.1016/j.icarus.2014.09.011

Froeschlé, C., Guzzo, M., & Lega, E., Graphical Evolution of the Arnold Web: From Order to Chaos. 2000, *Science*, **289**, 2108, DOI: 10.1126/science.289.5487.2108

Froeschlé, C., Lega, E., & Gonczi, R., Fast Lyapunov Indicators. Application to Asteroidal Motion. 1997, *Celestial Mechanics and Dynamical Astronomy*, **67**, 41, DOI: 10.1023/A:1008276418601

Gallardo, T., Atlas of the mean motion resonances in the Solar System. 2006, *Icarus*, **184**, 29, DOI: 10.1016/j.icarus.2006.04.001

Hanuš, J., Brož, M., Durech, J., et al., An anisotropic distribution of spin vectors in asteroid families. 2013, *Astronomy and Astrophysics*, **559**, A134, DOI: 10.1051/0004-6361/201321993

Kaasalainen, M. & Torppa, J., Optimization Methods for Asteroid Lightcurve Inversion. I. Shape Determination. 2001, *Icarus*, **153**, 24, DOI: 10.1006/icar.2001.6673

Kaasalainen, M., Torppa, J., & Muinonen, K., Optimization Methods for Asteroid Lightcurve Inversion. II. The Complete Inverse Problem. 2001, *Icarus*, **153**, 37, DOI: 10.1006/icar.2001.6674

Mahlke, M., Carry, B., & Mattei, P. A., Asteroid taxonomy from cluster analysis of spectrometry and albedo. 2022, *Astronomy and Astrophysics*, **665**, A26, DOI: 10.1051/0004-6361/202243587

Mainzer, A. K., Bauer, J. M., Cutri, R. M., et al., NEOWISE Diameters and Albedos V2.0. 2019, *NASA Planetary Data System*, DOI: 10.26033/18S3-2Z54

Margot, J. L., Pravec, P., Taylor, P., Carry, B., & Jacobson, S., Asteroid Systems: Binaries, Triples, and Pairs. 2015, in *Asteroids IV* (University of Arizona Press), 355–374

Nesvorny, D., Nesvorny HCM Asteroid Families V1.0. 2020, *NASA Planetary Data System*, urn:nasa:pds:ast.nesvorny.families::1.0

Nesvorný, D., Morbidelli, A., Vokrouhlický, D., Bottke, W. F., & Brož, M., The Flora Family: A Case of the Dynamically Dispersed Collisional Swarm? 2002, *Icarus*, **157**, 155, DOI: 10.1006/icar.2002.6830

Pravec, P., Fatka, P., Vokrouhlický, D., et al., Asteroid pairs: A complex picture. 2019, *Icarus*, **333**, 429, DOI: 10.1016/j.icarus.2019.05.014

Pravec, P., Scheirich, P., Kušnirák, P., et al., Photometric survey of binary near-Earth asteroids. 2006, *Icarus*, **181**, 63, DOI: 10.1016/j.icarus.2005.10.014

Rosaev, A., Resonant perturbation of a family of young asteroids associated with (5026) Martes. 2024, *arXiv e-prints*, arXiv:2403.03559, DOI: 10.48550/arXiv.2403.03559

Rosengren, A. J., Daquin, J., Tsiganis, K., et al., Galileo disposal strategy: stability, chaos and predictability. 2017, *Monthly Notices of the RAS*, **464**, 4063, DOI: 10.1093/mnras/stw2459

Simpson, G., Chong, E., Gerhardt, M., et al., Asteroid Lightcurve Analysis at the Oakley Southern Sky Observatory: 2012 August - October. 2013, *Minor Planet Bulletin*, **40**, 146

Smirnov, E. A., A new python package for identifying celestial bodies trapped in mean-motion resonances. 2023, *Astronomy and Computing*, **43**, 100707, DOI: 10.1016/j.ascom.2023.100707

Stephens, R. & Warner, B. D., The ALCDEF Database and the NASA SBN/PDS: The Perfect Merger. 2018, in AAS/Division for Planetary Sciences Meeting Abstracts, Vol. **50**, *AAS/Division for Planetary Sciences Meeting Abstracts #50*, 417.03

Sunshine, J. M., Connolly, H. C., McCoy, T. J., Bus, S. J., & La Croix, L. M., Ancient Asteroids Enriched in Refractory Inclusions. 2008, *Science*, **320**, 514, DOI: 10.1126/science.1154340

Tedesco, E. F., Binary Asteroids: Evidence for Their Existence from Lightcurves. 1979, *Science*, **203**, 905, DOI: 10.1126/science.203.4383.905

Tholen, D. J. 1984, Asteroid Taxonomy from Cluster Analysis of Photometry., PhD thesis, University of Arizona

Todorović, N., The precise and powerful chaos of the 5:2 mean motion resonance with Jupiter. 2017, *Monthly Notices of the RAS*, **465**, 4441, DOI: 10.1093/mnras/stw3070

Todorović, N., Mapping of the asteroid families. 2020, in *IAU General Assembly*, 17–18

Todorović, N. & Novaković, B., Testing the FLI in the region of the Pallas asteroid family. 2015, *Monthly Notices of the RAS*, **451**, 1637, DOI: 10.1093/mnras/stv1003

Vchkova Bebekovska, E., Todorović, N., Kostov, A., Donchev, Z., & Borisov, G., The Physical and Dynamical Characteristics of the Asteroid 4940 Polenov. 2021, *Serbian Astronomical Journal*, **202**, 39, DOI: 10.2298/SAJ2102039V

Vernazza, P., Lamy, P., Groussin, O., et al., Asteroid (21) Lutetia as a remnant of Earth's precursor planetesimals. 2011, *Icarus*, **216**, 650, DOI: 10.1016/j.icarus.2011.09.032

Vernazza, P., Zanda, B., Binzel, R. P., et al., Multiple and Fast: The Accretion of Ordinary Chondrite Parent Bodies. 2014, *Astrophysical Journal*, **791**, 120, DOI: 10.1088/0004-637X/791/2/120

Viikinkoski, M., Hanuš, J., Kaasalainen, M., Marchis, F., & Ďurech, J., Adaptive optics and lightcurve data of asteroids: twenty shape models and information content analysis. 2017, *Astronomy and Astrophysics*, **607**, A117, DOI: 10.1051/0004-6361/201731456

Vokrouhlický, D., Bottke, W. F., & Nesvorný, D., Forming the Flora Family: Implications for the Near-Earth Asteroid Population and Large Terrestrial Planet Impactors. 2017, *Astronomical Journal*, **153**, 172, DOI: 10.3847/1538-3881/aa64dc

Warner, B. D. 2016, *A Practical Guide to Lightcurve Photometry and Analysis* (Springer Cham)

Warner, B. D., Harris, A. W., & Pravec, P., The asteroid lightcurve database. 2009, *Icarus*, **202**, 134, DOI: 10.1016/j.icarus.2009.02.003

Zappala, V., Cellino, A., Barucci, A. M., Fulchignoni, M., & Lupishko, D. F., An analysis of the amplitude-phase relationship among asteroids. 1990, *Astronomy and Astrophysics*, **231**, 548